LATVIAN JOURNAL of PHYSICS and TECHNICAL SCIENCES

ISSN 0868 - 8257

5

(Vol. 55)

2018

SATURS

CONTENTS

СОДЕРЖАНИЕ

LATVIAN JOURNAL of PHYSICS and TECHNICAL SCIENCES

LATVIJAS FIZIKAS un TEHNISKO ZINĀTŅU ŽURNĀLS

ЛАТВИЙСКИЙ ФИЗИКО-ТЕХНИЧЕСКИЙ ЖУРНАЛ

Published six times a year since February 1964
Iznāk sešas reizes gadā kopš 1964. gada februāra
Выходит шесть раз в год с февраля 1964 года

5 (Vol. 55) • 2018

RĪGA

INDEKSĒTS (PUBLICĒTS) | INDEXED (PUBLISHED) IN

www.scopus.com
www.sciendo.com
EBSCO (Academic Search Complete, www.epnet.com), INSPEC (www.iee.org.com).
VINITI (www.viniti.ru), Begell House Inc/ (EDC, www.edata-center.com).

Izdevējs: Fizikālās enerģētikas institūts,
Reģistrācijas apliecība Nr. 0221
Redakcija: Krīvu iela 11, Rīga, LV-1006
Tel. 67551732
e-pasts: ezerniec@edi.lv
Interneta adrese: www.fei-web.lv

sciendo

LATVIAN JOURNAL OF PHYSICS
AND TECHNICAL SCIENCES
2018, N 5

DOI: 10.2478/lpts-2018-0031

PHYSICAL AND TECHNICAL ENERGY PROBLEMS

RISK TREATMENT AND SYSTEM RECOVERY ANALYSIS OF GAS SYSTEM OF GAS AND ELECTRICITY NETWORK OF LATVIA

L. Zemite[1], A. Kutjuns[1], I. Bode[1], M. Kunickis[2], N. Zeltins[3]

[1]Riga Technical University,
Faculty of Power and Electrical Engineering, Institute of
Industrial Electronics and Electrical Engineering,
12-1 Azenes Str., Riga, LV-1048, LATVIA
[2]AS Latvenergo,
12 Pulkveza Brieza Str., Riga, LV-1230, LATVIA
[3]Institute of Physical Energetics
11 Krivu Str., Riga, LV-1006, LATVIA

The Latvian natural gas system is interconnected with transmission networks located in Lithuania, Estonia and Russia. Natural gas commercial metering is provided by GMS "Karksi" (Estonia) and by GMS "Kiemenai" (Lithuania). Natural gas is supplied to all larger urban areas in Latvia. Natural gas is supplied to Latvia along the Latvian–Russian pipeline only during the warm period of the year (April–September), and it is accumulated in the underground gas storage facility in Incukalns. During winter, gas from the underground facility is delivered to Latvian customers, as well as transmitted to Estonia and back to Russia. There is also a connection to Lithuania. Out of the gas supply disruption risks that are assessed at different levels, the essential one with a trans-border impact potential consists in the insufficient technical capacity of Incukalns UGS. Given the current technical possibilities, IUGS cannot pass the gas volume required for the Baltic States to compensate the gas supply deficit. The paper performs system recovery analysis after selected critical events. The paper provides a report describing the steps to be followed in order to restore the gas transmission system to normal operation after selected critical events. A very significant region of the power system of Latvia is the central part of Latvia and Riga region, where both of Riga CHPs, as well as Riga HPP, is located. The restoration time of the gas system of Latvia depends on the gravity of the situation and damage in the gas system and may range from several hours to several days.

Keywords: critical infrastructure, gas system, risk assessment

1. INTRODUCTION

The Latvian natural gas system is interconnected with transmission networks located in Lithuania, Estonia, and Russia. Natural gas commercial metering is provided on the Latvian–Estonian border by GMS "Karksi" (Estonia), on the Latvian–Lithuanian border GMS "Kiemenai" (Lithuania). Natural gas is supplied to all larger urban areas in Latvia.

Natural gas is supplied to Latvia along with the Latvian–Russian pipeline only during the warm period of the year (April–September), and it is accumulated in the underground gas storage facility in Incukalns. During winter, gas from the underground facility is delivered to Latvian customers, as well as transmitted to Estonia and back to Russia. There is also a connection to Lithuania. Incukalns UGS started its operation in 1968. Incukalns UGS is used not only for customers in Latvia but also for the needs of consumers in Estonia, Lithuania, and Northwest Russia, thus securing reliable gas supply for the whole region [1].

2. POSSIBLE EVENTS THAT COULD CAUSE GAS SYSTEM ISOLATION

In case of an incident on any of the gas transmission pipelines leading to a situation when the supply of natural gas to consumers is limited or disrupted, the impact of the situation depends on such conditions as:

- Natural gas supply season and direction (summer/winter; pumping in/out of Incukalns underground gas storage);
- The possible places of gas pipeline damage (presence/absence of parallel gas pipeline; blind-end gas pipeline; presence/absence of trans-border connection);
- The current operating mode of the natural gas supply system (natural gas working pressure and distribution of natural gas reserve in the gas pipeline system);
- The actual natural gas demand in Latvia, its neighboring countries and in the Baltic region as a whole [2], [3].

The average natural gas consumption on a cold winter day is 10...13 million m^3. Since the amount of working (active) gas in Incukalns underground gas storage is 2.35 billion m^3 and the maximum pumping-out amount reaches 30 million m^3 per day, the storage has a sufficient additional amount of natural gas, which is used in emergency situations. Latvia's main gas pipelines constitute part of the natural gas supply system of the Baltic countries. For the case if the supply of natural gas from Incukalns underground gas storage is disrupted, Latvia has the possibility to receive alternative natural gas supplies from Russia: in winter, up to 2 million m^3 per day (directly); in summer, up to 20 million m^3 per day (directly); 6.48 million m^3 per day by way of transit via Lithuania. Alternative supplies of natural gas are also possible from Klaipeda liquefied natural gas terminal in Lithuania, which started its operation on 1 January 2015 [3], [4].

A more detailed description of the main risks related to gas pipelines is presented in Task 1.2. The following three scenarios of consequences are analysed:

- Natural gas flow disruption from Incukalns UGS in winter;
- Natural gas flow disruption from Russia in winter (GMS "Kotlovka");
- Natural gas flow disruption from Russia in winter (GMS "Kotlovka" and CS Izborsk) [3], [4].

Latvia has regulations regarding gas supply limitation. Depending on supply limitation, three stages of limitation are defined: I–7…12 %, II–12…17 %, III–above 17 %. There are 3 groups of customers and depending on the stage, the limitations for each group of customers are determined as percentage [5].

2.1. Disruption of Gas Supply from Incukalns UGS

During the winter season, natural gas supply to Latvia, Estonia and the Western part of Pskov Region of the Russian Federation is ensured from Incukalns UGS. The daily natural gas withdrawal capacity from Incukalns UGS is 24 million m^3, half of which is allocated to consumers in Latvia, while Russia and Estonia each get 6 million m^3 daily. For the case if gas supply from Incukalns UGS is lost, alternative gas supplies are available (Fig. 1):

- The maximum available supply from Russia to Latvia through GMS "Korneti" – 4.0 million $m^{3/}$day;
- The maximum available supply from Lithuania to Latvia through GMS "Kiemenai" – 6.5 million $m^{3/}$day;
- From Russia, there are no other gas supply routes.

Gas flow rearrangement:

- Disruption of the gas flow from Latvia to Russia;
- Disruption of the gas flow from Latvia to Estonia;
- Rearrangement of the gas flow from Russia to Estonia;
- Rearrangement of the gas flow from Russia to Latvia;
- Rearrangement of the gas flow from Latvia to Lithuania.

Short-term gas supply limitations for users in Latvia during the winter season in case of Incukalns UGS failure are analysed for 3 user groups depending on the scale of gas supply disruption [4], [6].

Taking into account the technical limits of natural gas supply, in case of disruption of natural gas supply from Incukalns UGS, rearrangement of the natural gas flow will not result in the daily demand for natural gas being met – the natural gas shortage in Latvia will make 6 million cubic meters per day.

As regards the operation of the compressor stations, the present paper contains those units of process equipment situated in the base territory, defects or incidents on which may lead to a natural gas leak and, consequently, a gas explosion or fire in case of ignition. The amount and spread of the incident consequences are influenced by the nature of the incident and the amount of leaked gas, which in turn depends on the possibilities of timely leak detection and disruption of gas supply to the damaged equipment unit or assembly. In the simulation of the incident consequences, the worst-case situation has been presented, i.e., a case when the safety system fails

to come into action, which means that, according to the Dutch guidelines for the assessment of quantitative risk, a 30-minute leak is considered, or a leak that lasts until complete emptying of the tank [2], [4], [7].

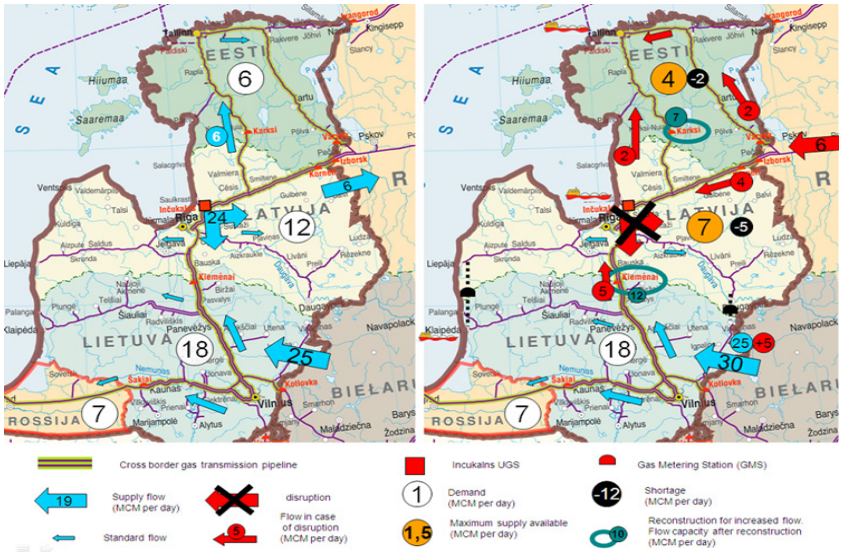

Fig. 1. Gas supply of the Baltic States in case of the scenario of gas supply disruption from Incukalns UGS.

In a gas compressor, there may be a leak from the compressor through a damaged place with a diameter equal to the diameter of the largest pipeline connected to the equipment unit; also a leak is considered from the compressor through a damaged place with a diameter equal to 10 % of the diameter of the largest pipeline connected to the equipment unit.

As regards the gas pipelines, two gas leak scenarios are analysed: (1) a leakage from a pipeline through a damaged place with a diameter equal to 1/3 of the nominal diameter of the pipeline; (2) a complete disruption of the pipeline. For pipeline incidents, both instantaneous ignition and delayed ignition of the gas are considered; hence, the incident consequences have been described both for a jet-type fire and a gas cloud explosion/fire [3], [5], [8].

Separately, as part of pressure tanks, dust catchers and dividing filters are considered, evaluating incident consequences according to the Dutch recommendations for assessing quantitative risk: (1) in case of tank emptying within ten minutes; (2) in case of instantaneous emptying of the tank. In case of a gas leak, both instantaneous ignition and delayed ignition of the leaked gas are possible.

For the gas collection stations (GCSs), incident scenarios related to the operation of gas pipelines as well as separators are considered. In connection with the GCSs, scenarios related to the operation of the methanol facilities have also been analysed. For the gas pipelines, two leak scenarios have been analysed: (1) a leak from the pipeline through a damaged place with a diameter equal to 1/3 of the nominal diameter of the pipeline; (2) a complete disruption of the pipeline. Calculations show that further spread of the adverse influence in the case of an incident involving

the pressure tanks of a GCS might be expected in case of instantaneous emptying of gas and delayed ignition; yet, considering the properties of the gas and its amount in the considered tanks, the possibility of such an incident is to be deemed only hypothetical. A much more typical incident could be tank damage accompanied by gas leakage, the worst type of incident consequence being a jet fire. Calculations show that the adverse influence of a jet fire in case of tank emptying over ten minutes might extend up to 20 meters from the damaged place.

The risk assessment includes gas-pumping pipelines between compressor stations and GCSs as well as between GCSs and the wells of the gas storage. As regards the transport pipelines, two scenarios have been considered according to the Dutch guidelines for the assessment of quantitative risk [1]: (1) a leak from the pipeline through a damaged place with a size equal to 10 % of the nominal diameter of the pipeline, (2) complete disruption of the pipeline. Likewise other natural gas leak scenarios, also regarding the pipelines, the paper considers a gas leak with instantaneous ignition and subsequent development of a jet fire as well as a delayed ignition of the leaked gas with a potential development of gas cloud explosions/fire [9], [10].

For Incukalns UGS, the document considers spread of the influence of gas cloud explosion and jet fire in the following emergency cases: (1) a large-scale leak from a well (a leak from a damaged place with a size equal to the diameter of the extraction column) – vertical leakage; (2) a leak from a well (a leak from a well through a damaged place with a diameter equal to 10% of the diameter of the extraction column) –vertical leakage; (3) a leak from a well (a leak from a well through a damaged place with a diameter equal to 10% of the diameter of the extraction column) – horizontal leakage. The worst-case course of development, both for the old wells and the reconstructed ones, is an incident when the safety system fails to come into action and the leakage of gas from the well lasts for thirty minutes and longer [11]–[13].

3. RESTORATION OF THE GAS SYSTEM OF LATVIA

Readiness for an emergency situation is planned on the basis of the following:

- The results of the identification and assessment of industrial incidents (Safety Report, other documents (including inspections, monitoring, equipment checks)),
- Preventive risk-diminishing measures;
- Emergency action plans for emergency cases checked in theoretical and practical training and reviewed.

The *emergency communications plan* indicates the co-operation services that are involved in the case of emergency situations and incidents in the Republic of Latvia and determines the co-operation partners outside Latvia in cases of emergency situations and incidents [14]–[16].

The most important actions in case of fire are calling the rescue service and performing fire containment works. If the incident has taken place, the most important thing to do is timely stopping of the technological process so as to diminish the scale of the incident (catastrophe) and its potential consequences. Mass notification is to be done immediately [16], [17].

Below follow the possible solutions for the case of an incident involving the gas transmission pipelines, along with their influence on the neighbouring member countries (Estonia, Lithuania):

- For the gas pipelines with interconnections to Russia (Valday–Pskov–Riga) and Lithuania (Riga–Vilnius) it is possible to change the natural gas supply directions for reverse supply/reception of natural gas (in the Vireši–Tallinn interconnection with Estonia); it will be possible to use the reverse supply possibilities after the completion of the European project of common interest "Enhancement of Estonia-Latvia Interconnection (PCI project 8.2.2)" in 2021). Taking into account that the natural gas supply systems of the neighbouring countries have their own interconnections with Russia and that there is a liquefied natural gas terminal in Lithuania, the potential change of the gas supply direction to ensure reverse supply of natural gas would have minimum impact on the natural gas supply reliability in the neighbouring member states;
- In summer, there is a possibility to interrupt the supply of natural gas from Russia via the Valday–Pskov–Riga gas pipeline and to rearrange Incukalns underground gas storage to pumping-out mode and ensure the supply of natural gas to the consumers in Latvia without significant influence on the natural gas supply reliability in the neighbouring member states;
- Regarding the blind-end gas pipelines (Riga–Daugavpils, and Iecava–Liepaja), the situation depends on the possible location of the damage; the influence is mainly determined by the actual natural gas demand, the gas pressure in the disconnected gas pipeline section and the total remaining natural gas reserve amount. This solution leads to the risk of an increased influence on the natural gas supply systems of the neighbouring member countries;
- Depending on the extent of damage, the T.D.Williamson gas pipeline blocking system can be used, building a local bypass line around the damaged place to ensure natural gas supply as a temporary arrangement, with minimum influence on the natural gas supply reliability of the neighbouring member countries;
- Within approximately 24 hours, it is possible to ensure supply of liquefied natural gas tanks from Poland and other producers of liquefied natural gas [8], [16], [17].

3.1. Emergency Containment and Elimination Plan

The report should include a hypothetical scenario of a complete loss of gas in the transmission network. Losses of gas are possible only in some places and territories. Automatic shut-off valves are set up in all GRS. Valves are working the case of losses of gas and/or power supply. Therefore, it is possible to evaluate gas loss in separate cases or territories. Firstly, personnel has to check whether the gas leaks and the system phase are emptied. The next step is to restore the damaged site. Then it is necessary to open the closures and check the system for leakage and pressure

resistance. Hypothetically, if the pressure in the transmission system drops to 1 bar, then it is possible to restore the pressure throughout the transmission system within one day [1].

3.1.1. Fires and Explosions

The possible causes of the emergency are ignition or an explosion at a gasified facility, etc. The sequence of actions is as follows:

1.1. Accept the emergency call and inform the caller about the required safety measures to be taken before the arrival of the emergency service team.

1.2. Register the emergency call and create an emergency call registering the card.

1.3. Inform the emergency service team about the nature of the emergency situation and prepare the required documentation. Depart for the emergency location within five minutes.

1.4. Discontinue gas supply to the affected facility.

1.5. Fence off a safety area by means of barrier belts and warning signs and provide it with surveillance, prohibiting smoking, the use of open fire, switching on and off of electrical switches, the use of bells and other electrical appliances, in co-operation with the State Fire and Rescue Service.

1.6. By using a gas concentration meter (further referred to as "analyser"), check the gas concentration within a radius of 50 meters in cellars, staircases, living accommodations and underground utility wells.

1.7. Create an emergency call registering the card and draw up a technical protocol, along with other required documentation [18].

3.1.2. Gas Odor from the Underground Gas Pipeline

The possible causes of the emergency are as follows: a gas leak from a disrupted underground gas pipeline; a gas leak at a corroded or welded place, from an underground well-less shutoff device, etc. The sequence of actions is as follows:

1.1. Accept the emergency call and inform the caller about the required safety measures to be taken before the arrival of the emergency service team.

1.2. Register the emergency call and create an emergency call registering the card.

1.3. Inform the emergency service team about the nature of the emergency situation and prepare the required documentation. Depart for the emergency location within five minutes.

1.4. Determine the safety area based on the gas odor or measured gas concentration; delimit it by means of barrier belts and warning signs. Ensure surveillance for the safety area, prohibiting smoking and the use of open fire and electrical appliances.

1.5. By using a gas concentration meter (further referred to as "analyser"), check the gas concentration within a radius of 50 meters in cellars, staircases, underground utility wells. Determine the safety area more precisely and make changes according to the situation.

1.6. By using the gas analyser, determine the gas leakage location on the underground gas pipeline; if required, the leak is sought for by means of check boring.

1.7. If possible, disconnect the damaged pipeline section or perform pressure lowering.

1.8. If it is required to start uncovering the damaged pipeline section (excavation), representatives from the other organisations operating the underground utilities are summoned to the emergency site.

1.9. The damaged section is uncovered and the leak is contained or eliminated. The gas consumers are notified about the prospective gas supply disruption or pressure lowering.

1.10. Draw up the required documents about the handing over of the facility to a repair team for reconstruction [18].

3.1.3. Changes in Gas Pressure or Disrupted Gas Supply

The possible causes of the emergency are as follows: damage to the gas pressure regulator; clogging caused by condensate, snow, or ice; mechanical clogging of the gas pipelines; a closed shutoff device on the gas pipeline; etc. The sequence of actions is as follows:

1.1. Accept the emergency call and inform the caller about the required safety measures to be taken before the arrival of the emergency service team.

1.2. Register the emergency call and create an emergency call registering the card.

1.3. Inform the emergency service team about the nature of the emergency situation and prepare the required documentation. Depart for the emergency location within five minutes.

1.4. Determine the actual cause of the changes in the gas pressure conditions by performing monitoring of the exit pressure related to the emergency location as well as monitoring of the pressure before the gas equipment of the caller.

1.5. Restore the gas pressure in the pipelines according to the prescribed pressure conditions.

1.6. If it is impossible to restore the gas pressure according to the prescribed pressure conditions:

1.6.1. Discontinue gas supply and warn the consumers about the discontinuation of gas supply during the repair period.

1.6.2. Summon to the emergency location an additional repair team with the required equipment.

1.7. Draw up the required documents [16].

3.2. Starting to Use the Pipelines

A pipeline may only be commissioned after a pressure check. If a pipeline section is commissioned or decommissioned, gas pipeline flow-out may be used. The flow-out procedure has been completed if the results of the measurements made at the flow-out place show a safe and acceptable gas concentration. Before the check, it is necessary to check the cleanliness and (if required) quality of the pipeline section. The pipeline section has to be cleaned by means of a piston. In order to clean the pipe and (if required) check its quality, it is necessary to pass the piston through each of the blocked pipeline sections a number of times. The piston moving speed has to be monitored by means of a manometer.

The pressure test has to be used to make sure about the strength and leakproofness of the pipeline. Testing the pressure, water can be used as the fluid; it has to be clean and (if required) with a corrosion inhibitor added. In order to prevent the formation of air pockets, the pipe has to be filled by using pistons. After the filling has been completed, it is necessary to allow the water in the pipeline sections to settle. Before starting the test, it is necessary to determine the water pressure to be applied as well as the locations of the metering devices and their characteristic quantities. At the places where the manometers are located, sheds have to be installed.

The minimum duration of the strength test is fifteen minutes. The pipe strength test has to be conducted, starting from an actual maximum pressure that exceeds the maximum working pressure 1.15 times in the lowest pipeline section to be tested.

The pressure used in the strength test must not exceed the pressure that causes permanent deformations. During the test, the monitored pressure must not form considerable pressure drops. The test may be conducted during the stabilization period before the leakproofness test. A hydrostatic test can be conducted. Air or an inert gas is acceptable as the testing medium if adequate safety measures are taken and the pressure-volume product is kept within certain limits. The leakproofness test may be conducted together with the strength test. The pressure used in the leakproofness test must not be higher than the pressure used in the strength test. At the beginning of the leakproofness test, the pressure must not be lower than the working pressure. The duration of the test may not be shorter than 24 hours.

A hydrostatic test may be conducted. Air or an inert gas is acceptable as the testing medium if adequate safety measures are taken and the pressure-volume product is kept within certain limits. Before the leak proneness test, it is necessary to make sure that the amount of air in the pipe is so small that it will not influence the testing results. The pipe is to be considered leak proof if the temperature and pressure measurements show that the volume of the testing medium has remained unchanged during the testing.

If the test has yielded satisfactory results, the pipeline has to be cleaned from the water. The piston devices have to be passed through the pipeline as many times as is necessary to clean it from the water.

The putting into operation has to be conducted in such manner as to ensure elimination of all the gas/air mixtures that have been formed and to prevent any air from remaining in the pipeline. After that, the pressure under the checking pipeline has to be increased to reach a normal working pressure.

Before repeated commissioning, it is necessary to make sure that the work has been performed and checked in a proper way. Special attention has to be paid to welding works, leak proneness, coating integrity and cathodic protection. During the repeated filling, the pressure must not exceed the permissible limit values [19].

4. CONCLUSIONS

Out of the gas supply disruption risks that are assessed at different levels, the essential one with a trans-border impact potential consists in the insufficient technical capacity of Incukalns UGS. Given the current technical possibilities, IUGS cannot pass the gas volume required for the Baltic States to compensate the gas supply deficit.

From the point of view of Latvian gas supply system security, the highest priority should probably be attributed to the necessity to renew the technical resources of the gas transmission pipeline Iecava–Liepaja, as well as to construct the Latvian and Lithuanian gas supply system gas transmission pipeline junctions Liepaja–Klaipeda, and Daugavpils–Visaginas. As GMS "Kiemenai" is considered the bottleneck of the region's gas supply, in order to avoid useless investments, it would be required to make a survey regarding the increase of optional interconnection capacity. Estonia, in case of maximum gas demand, is not able to meet its gas needs only from Russia via pipelines; rather, it also has to receive gas from Latvia. Besides, the pressure in Estonia's gas system depends on external sources and pressure limitations in separate parts of the system limit the options in crisis situations.

A very significant region of the power system of Latvia is the central part of Latvia and Riga region, where both of Riga CHPs, as well as Riga HPP, is located.

The restoration time of the gas system of Latvia depends on the gravity of the situation and damage in the gas system and may range from several hours to several days.

As GMS Kiemenai is considered the narrowest place of region gas supply, in order to avoid useless investments, it would be required to make a survey on the increase of optional inter-connection capacity. Estonia, in case of maximal gas demand, is not able to provide the necessity for gas only from Russia by pipelines, but it has to receive gas also from Latvia. Besides, the pressure in Estonian gas system depends on the external sources and pressure limitations in separate system parts limit the options in crisis situations.

From the perspective of Latvian gas supply system security, it is necessary to renew the technical resources of the transmission gas pipeline Iecava – Liepaja, as well as the construction of Latvian and Lithuanian gas supply system transmission gas pipeline junction Liepaja – Klaipeda and Daugavpils – Visagina.

REFERENCES

1. Latvijas dabasgāzes apgādes drošība (2015). *PSI "Risks un audits" SIA*. Rīga.
2. Republic of Latvia Cabinet Regulation No. 496. (2010). *Procedures for the Identification of Critical Infrastructures, Including European Critical Infrastructures and Planning and mplementation of Security Measures.* [Online]. [Acessed: 9 March 2017] https://likumi.lv/doc.php?id=212031.

3. JSC Latvijas Gāze, & JSC Conexus Baltic Grid. Unpublished materials.
4. Niedrite, I., Kreslins, A., Davis, A., & Zeltins, N. (2013). Security of gas supply risk assessment alternatives. In *Proceedings of 22nd World Energy Congress*, (No. 820, pp. 14), 17 October 2013. Daegu, Korea.
5. Committee for the Prevention of Disasters. (1999). *Guidelines for Quantitative Risk Assessment*, "Purple Book" CPR 18E, Hague.
6. Umbach, F. (2010). Global Energy Security and the Implications for the EU. *Energy Policy, 38*(3), 1229–1240.
7. Jansons, L., Zeltins, N., & Savickis J. (2016). The Latvian UGS potential and alternative use of underground geological structures. e-Proceedings of 23rd World Energy Congress, 9–13 October 2016, Lütfi Kırdar Congress Center, Istanbul. ISBN: 978-605-89548-9-2.
8. Regulation of the European Parliament and of the Council concerning measures to safeguard the security of gas supply and repealing regulation (EU) No 994/2010, {SWD(2016) 26 final}. [Accessed: 9 March2017]
9. Ivanova, P., Sauhats, A., & Linkevičs, O. (2016). Towards optimization of combined cycle power plants' start-ups and shut-down. In *57 International Scientific Conference on Power and Electrical Engineering of Riga Technical University (TUCSON)*, Latvija, Riga.
10. Ivanova, P., Sauhats, A., Linkevičs, O., & Balodis, M. (2016). Combined heat and power plants towards efficient and flexible operation. In *IEEE 16th International Conference on Environmental and Electrical Engineering (EEEIC),* 7–10 June 2016, Florence, Italy.
11. The Role of Underground Gas Storage for Security of Supply and Gas Market. (2010). Occasional Paper. Energy Charter Secretariat.
12. Szikszai, A., & Monforti, F. (2011). GEMFLOW: A time-dependent model to assess responses to natural gas supply crises. *Energy Policy, 39*(9), 5129-5136.
13. Parks, P., Kopustinskas, V., & Masera, M. (2015). Probabilistic modeling of security of supply in gas networks and evaluation of new infrastructure. *Reliab. Eng. and Syst. Saf. 144*, 254–264.
14. Zemite, L., Gorobecs, M., Smats, A., Jasevics, A., & Shevchenko's, A. (2017). Genetic algorithm for optimization of power switch allocation in distribution network. In *17th IEEE International Conference on Environment and Electrical Engineering and 1st IEEE Industrial and Commercial Power Systems Europe*, *EEEIC / I and CPS Europe 2017.*
15. Zemite, L., Gerhard, J., Gorobetz, M., & Levchenkov, A. (2016). Optimization of distribution system reliability. In *the International Conference on Environment and Electrical Engineering*.
16. Zemite, L., Bode, I., Zeltins, N., Kutjuns, A., & Zbanovs, A. (2018). Analysis of the power system damage hazard from the point of view of the gas supply system. In *International Conference on Environment and Electrical Engineering*.
17. Moshkin, I., & Sauhats, A. (2016). Solving district heating problems by using cooperative game theory methods. In *Proceedings of 16th International Conference on Environment and Electrical Engineering.*
18. Zemite, L., Kutjuns, A., Bode, I., Kunickis, M., & Zeltins, N. (2018). Consistency analysis and data consultation of gas system of gas-electricity network in Latvia. *Latvian Journal of Physics and Technical Sciences*, *55*(1)., 22–34.
19. Zemite, L., Gerhard, J., Gorobetz, M., & Levchenkov, A. (2015). Optimization of distribution systems reliability with the stochastic behavior. In 56th International Scientific Conference on Power and Electrical Engineering of Riga Technical University, RTUCON 2015.

LATVIJAS GĀZES – ELEKTROENERĢIJAS TĪKLU GĀZES SISTĒMAS RISKU NOVĒRTĒJUMS UN SISTĒMAS ATJAUNOŠANAS ANALĪZE

L. Zemīte, A. Kutjuns, I. Bode, M. Kuņickis, N. Zeltiņš

Kopsavilkums

Latvijas dabasgāzes sistēma ir savstarpēji savienota ar Lietuvas, Igaunijas un Krievijas pārvades tīkliem. GMS "Karksi" (Igaunija), GMS "Kiemenai" (Lietuva) tiek nodrošināta dabasgāzes mērīšana. Dabasgāze tiek piegādāta visām lielākajām Latvijas pilsētām. Dabasgāze tiek piegādāta uz Latviju pa Latvijas un Krievijas cauruļvadiem tikai vasaras sezonā (aprīlis-septembris), un tā tiek uzkrāta Inčukalna pazemes gāzes krātuvē. Ziemas laikā gāze no pazemes gāzes krātuves tiek piegādāta Latvijas klientiem, kā arī piegādāta uz Igauniju un atpakaļ uz Krieviju. Ir arī savienojums ar Lietuvu. No gāzes piegādes traucējumu riskiem, kurus novērtē dažādos līmeņos, būtiskākais ar pārrobežu ietekmes potenciālu ir Inčukalna PGK nepietiekamā tehniskā kapacitāte. Ņemot vērā pašreizējās tehniskās iespējas, IPGK nevar nodrošināt gāzes apjomu, kas nepieciešams Baltijas valstīm, lai kompensētu gāzes piegādes deficītu. Rakstā tiek veikta sistēmas atjaunošanas analīze pēc izvēlētiem kritiskiem notikumiem. Šajā rakstā ir sniegts pārskats par pasākumiem, kas jāievēro, lai pēc izvēlētiem kritiskiem notikumiem atjaunotu gāzes pārvades sistēmas normālu darbību. Ļoti nozīmīgs Latvijas energosistēmas reģions ir Latvijas centrālā daļa un Rīgas reģions, kur atrodas gan Rīgas TEC, gan Rīgas HES. Latvijas gāzes sistēmas atjaunošanas laiks ir atkarīgs no situācijas nopietnības un bojājumiem gāzes sistēmā un var būt no vairākām stundām līdz vairākām dienām.

24.04.2018.

sciendo

LATVIAN JOURNAL OF PHYSICS
AND TECHNICAL SCIENCES
2018, N 5

DOI: 10.2478/lpts-2018-0032

ACCURATE MODEL FOR TEMPERATURE DEPENDENCE OF SOLAR CELL PERFORMANCE ACCORDING TO PHONON ENERGY CORRECTION

Y. Tiandho[1,2]*, W. Sunanda[1,3], F. Afriani[2], A. Indriawati[1,2], T. P. Handayani[4]

[1]Research Center for Energy and Information Technology,
Universitas Bangka Belitung, Indonesia
[2]Department of Physics, Universitas Bangka Belitung, Indonesia
[3]Department of Electrical Engineering, Universitas Bangka Belitung, Indonesia
[4]Department of Information System,
Universitas Muhammadiyah Gorontalo, Indonesia
*e-mail: yuant@ubb.ac.id

In many experiments, it has been reported that the performance of solar cells decreases with increasing temperature. This effect arises due to an increase in the intrinsic carrier concentration of material that directly affects the reverse saturation currents (J_0). As a result, the open circuit voltage which is inversely proportional to J_0 will decrease quite rapidly with increasing temperature. The intrinsic carrier concentration is determined by the bandgap energy of a material and its temperature. The Varshni relationship is a relation for the variation of the bandgap energy with temperature in semiconductors that has been used extensively in the model of a solar cell performance. But the problem is the Varshni relation just calculates the contribution of the vibrational part at the temperature, which is much greater than the Debye temperature. These works proposed a model of temperature dependence of solar cell performance that involves phonon energy correction and electron-phonon coupling interaction. This correction is applied because the electron-phonon coupling interaction is an intrinsic interaction of semiconductors. The existence of interaction cannot be avoided either experimentally or theoretically. The proposed model is compared with experimental data, which have fairly high accuracy.

Keywords: *phonon, semiconductor, solar cell, temperature*

1. INTRODUCTION

Being concerned about the limited sources and pollution effects of fossil fuels, various countries all over the world have been developing renewable energy sources [1], [2]. The use of solar cells, which are devices that can directly convert sunlight into electrical energy, provides huge potential in both economic and environmental

benefits [3]. In addition, the solar cell systems also provide easy installation so that they can be used to supply electricity for people who do not have access to the main electrical source [4].

Reliability is one of the important factors in the selection of solar cells besides their efficiency [5]. Solar cells that cannot survive in extreme environmental conditions will have an impact on increased maintenance costs that will increase the electricity price. There are several environmental factors that affect the performance of solar cells such as dust [6], humidity [7] and temperature [8]. However, the temperature is the most important factor because in terrestrial application, solar cells are generally exposed to temperature ranging from 15 °C to 50 °C. In addition, the use of solar cells has covered a wider field such as space and concentrator systems that have higher temperatures [9].

Many studies have reported that the performance of solar cells decreases as temperature increases. The performance of solar cells is expressed by the characteristics of short circuit current density (J_{SC}), open circuit voltage (V_{OC}), fill factor (*FF*) and efficiency (η). Some solar cell models state that the working of solar cells is equivalent to a series of combinations of current sources (which are generated by light) with a diode [10]. Therefore, the value of solar cell performance parameters is related to a diode parameter. Some diode parameters of a solar cell are reverse saturation current density (J_O) and an ideal factor, which is related to the resistance. It has been shown that the V_{OC} has decreased with temperature even though J_{SC} has slightly improved. The temperature rise also causes a decrease in *FF* and η due to the significance of V_{OC} change to temperature. Many cases have reported that the temperature is not significant in changing the resistance but J_O is exponentially dependent on temperature [9], [10].

The temperature dependence of J_O arises from the relation between the saturation current density and the bandgap of a material. In literature, it is stated that parameter J_O contains the intrinsic carrier concentration variable of the semiconductor material n_i, i.e [11,9].,

$$J_o = qn_i^2\left(\frac{1}{N_D}\sqrt{\frac{D_p}{\tau_p}}+\frac{1}{N_A}\sqrt{\frac{D_n}{\tau_n}}\right), \tag{1}$$

where q is the elementary charge, D_P and D_n are the diffusion coefficients of holes and electrons, N_A and N_D are acceptor and donor constants, and τ_P and τ_n are the lifetime carriers of holes and electrons. Then n_i is expressed as a variable that depends on the band gap as [9]

$$n_i^2 = 4\left(\frac{2\pi kT\sqrt{m_n^* m_p^*}}{\hbar^2}\right)^3 \exp\left(-\frac{E_g}{kT}\right), \tag{2}$$

where T is temperature, m_n^* and m_p^* are effective mass of electrons and holes whereas k and $\hbar$ are Boltzmann constant and Planck constant. According to both equations, it is clear that the important factors in the calculation of J_O are strongly dependent on the bandgap and its temperature.

It has been reported that the energy of the semiconductor bandgap depends on temperature [12]–[14]. Higher temperature reduces its bandgap. Varshni proposes a formula that is often used to describe the dependence of the semiconductor bandgap on the temperature in a non-linear relation [12]

$$E_g(T) = E_g(0) - \frac{\alpha T^2}{(\beta + T)}\ , \tag{3}$$

where $Eg(0)$ is a bandgap energy at $T \approx 0$ K, and α and β are characteristic fitting parameters that depend on material type. This relation is also often used to describe the performance of solar cell that depends on temperature [8], [9]. In Varshni's model it is stated that the variation of bandgap energy with temperature is generated by two mechanisms: (1) a shift in the relative position of the conduction band and the valence band due to the dependence of lattice dilatation to temperature, and (2) the relative positioning of the conduction band and valence due to the dependence of the electron lattice interaction. Although the Varshni relation provides a good relationship on the bandgap energy (especially in the III-V and II-VI semiconductors), it cannot be generally applicable. The Varshni relation just calculates the vibrational parts at temperature, which is much higher than the Debye temperature. As an example, chalcopyrite compound is incompatible with Varshni relation [14].

Around the 1990s, O'Dennell and Chen proposed a model of the relationship between the bandgap energy and the temperature that involved the intrinsic interaction of a semiconductor called the electron-phonon interaction [14]. Through the relations which were formulated on the vibronic-based model, O'Dennell and Chen provided better correction of the bandgap energy-temperature relationship. In addition, they also calculated the thermodynamic functions, such as Gibbs energy, enthalpy and entropy from the electron-hole pair formation in semiconductors. Therefore, to improve the calculation of solar cell performance as a function of temperature and to eliminate the effect of β constants that may be unphysical, in this paper we propose a new model involving electron-phonon interaction. Experimental data verify the accuracy of the model.

2. MODELLING

When a solar cell is illuminated, only the photons having energy higher than the bandgap energy (E_g) can excite electrons and create electron-hole pairs. O'Dennell and Chen [14] proposed the model of the bandgap-temperature relations

$$E_g(T) = E_g(0) - S\langle\hbar\omega\rangle\left(\coth\left(\frac{\langle\hbar\omega\rangle}{2kT}\right) - 1\right), \tag{4}$$

where S is the coupling constant and $\langle\hbar\omega\rangle$ is the average phonon energy. Figure 1 shows the comparison between the Varshni relationship and the bandgap-temperature relationship based on phonon energy correction for the GaAs and Si semicon-

ductors. In this case, Si semiconductors have higher bandgap compared to GaAs. Based on comparison with experimental data, it appears that the phonon energy correction gives better results than Varshni relationship. In this model, it is clear that the semiconductor bandgap decreases with increasing temperature.

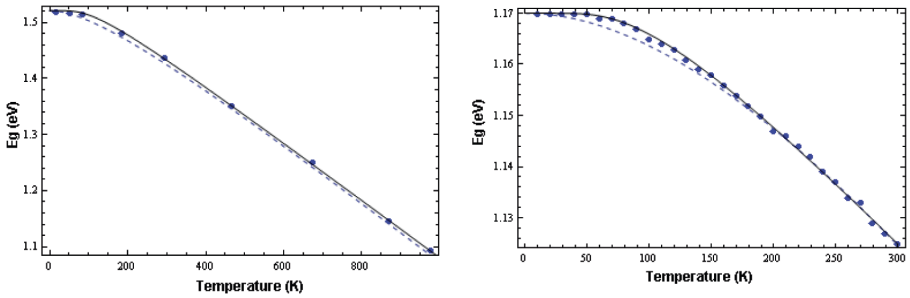

Fig. 1. Energy bandgap as a temperature function for the Varshni relation (dashed) and the phonon energy correction (line) in the experimental data of semiconductors (dots): (a) GaAs and (b) Si [14].

For a simple overview, an equivalent circuit of an ideal solar cell is the combination of a current source (the current generated by light) and a diode as shown in Fig. 2(a). The solar cell behaves similarly to diodes and its electrical characteristics are represented by the voltage-current density (current) curve (J-V curve) as shown in Fig. 2(b). The J-V curve characteristics of p-n junction solar cells under steady state illumination can be summarised in the exponential model,

$$J = J_L + J_0\left(e^{qV/AkT} - 1\right) \tag{5}$$

where J_L represents current density, V is the terminal voltage (developed across the junction voltage) and A is the ideal factor of the diode. This paper ignores the resistance of system because temperature changes do not change the resistance in the circuit significantly.

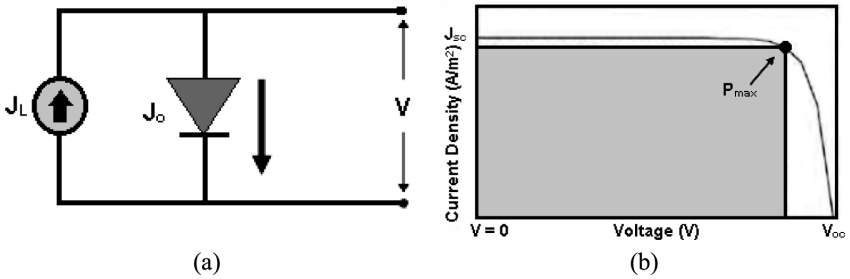

Fig. 2. (a) Equivalent circuit of an ideal solar cell and (b) J-V curve.

On the J-V curve it is possible to determine several variables related to solar cell performance such as J_{SC}, V_{OC}, P_{max}, FF, and efficiency. J_{SC} is a variable that

represents the short circuit current density that is the maximum value of the current density that occurs when the solar cell voltage is zero. V_{OC} is the open circuit voltage which is the maximum voltage when the current is zero. P_{max} is the maximum power produced by a solar cell with a value determined by the maximum J-V variables. The *FF* or fill factor is a variable associated with the ratio of P_{max} with the multiplication of V_{OC} and J_{SC}

$$FF = \frac{P_{\max}}{V_{OC} J_{SC}} \ . \tag{6}$$

Therefore, the efficiency of solar cell can be defined as ratio of P_{max} to input power

$$\eta = \frac{P_{\max}}{P_{in} Area} \text{ or } \eta = \frac{V_{OC} J_{SC} FF}{P_{in}} \ . \tag{7}$$

According to Eq. (5), it is stated that the V_{OC} is given by

$$V_{oc} = \frac{AkT}{q} \ln\left(\frac{J_{sc}}{J_0}\right), \tag{8}$$

where q is the charge of electrons. Basically, J_0 is a measure of the leakage or recombination of the minor carrier passing through the p-n junction in a reverse bias condition. Through Eqs. (1) and (2), the relationship between J_0 and temperature can be expressed by the relationship

$$J_0 = CT^3 \exp\left(-\frac{E_g}{mkT}\right), \tag{9}$$

where C is an empirical parameter that depends on the type of material and doping. The m is an empirical parameter that depends on the quality of material cells and junctions, for high purity monocrystalline material the m value is one. In [9], it is also stated that C is a constant that relates to the atom density of donor and acceptor, the diffusion constant of the minority carriers in regions p and n, the diffusion length of the minority carriers, the electron and hole masses, and the densities of conditions in the conduction band and valence. Nevertheless, through the expression in Eq. (9), it can be seen that the bandgap is inversely proportional to the saturation current density. Hence, substituting Eq. (9) with Eq. (4) and Eq. (8) lead produces the relation between temperature with V_{OC}

$$V_{oc} = \frac{AkT}{q} \ln\left(J_{sc} \Big/ CT^3 \exp\left(-\frac{E_g(0) - S\langle\hbar\omega\rangle\left(\coth\left(\langle\hbar\omega\rangle/2kT\right)-1\right)}{mkT}\right)\right). \tag{10}$$

The current density of J_{SC} is a variable that depends on the spectral irradiation of sunlight and in experimental experience the value of J_{SC} can be limited by reflection losses, electrical resistance losses, shadowing losses and recombination losses [9]. Basically, the formula of the J_{SC} is very complex, i.e., $J_{sc} = q\int_{h\nu=E_g}^{\infty}\left(dN_{ph}/dv\right)d\left(h\nu\right)$: where *Nph* is the photon density; and ν is the frequency of the photon, to obtain J_{SC} value and its derivative to the temperature explicitly, numerical analysis is used. Experiments regarding the determination of J_{SC} values for different types of solar cell materials have been reported by Green [16] for measurements under the AM 1.5G spectrum, while Wysocki and Rappaport [17] – for measurements under the AM 0G spectrum. The results show that it is safe to say that in general the AM 0G spectrum can produce J_{SC} higher than the AM 1.5 G spectrum for different types of solar cell materials such as Si, GaAs, CdTe, Ge, InP, and CdS [9].

Based on the definition described above, the temperature dependence of V_{OC} can be obtained through the relationship

$$\frac{dV_{oc}}{dT} = \frac{AkT}{q}\left(\frac{1}{J_{sc}}\frac{\partial J_{sc}}{\partial T} - \frac{1}{J_0}\frac{\partial J_0}{\partial T}\right) + \frac{V_{oc}}{T} \tag{11}$$

and the relationship between the dependence of the saturation current density J_0 and the temperature can be expressed as

$$\frac{\partial J_0}{\partial T} = 3CT^2\exp\left(-\frac{E_g}{mkT}\right) + CT^3\exp\left(-\frac{E_g}{mkT}\right)\left(\frac{E_g}{mkT^2} - \frac{1}{mkT}\frac{\partial E_g}{\partial T}\right). \tag{12}$$

According to[15], the definition of fill factor in Eq. (6) is modified as follows:

$$FF = \frac{V_m}{V_{oc}}\left(1 - \frac{F\left(\exp\left(\frac{qV_m}{kT}\right)-1\right)}{G\left(\exp\left(\frac{qV_{oc}}{kT}\right)-1\right)}\right), \tag{13}$$

where *F* and *G* are the parameters that arise from the relationship between V_m with J_m and V_{OC} with J_{SC}. Therefore, with simple modification V_m satisfies the relationship

$$\exp\left(\frac{qV_m}{BkT}\right)\left(1 + \frac{qV_m}{BkT}\right) = \frac{J_{sc}}{J_0} + 1 \ , \tag{14}$$

where *B* is an empirical parameter. Explicitly, V_m can be expressed as follows:

$$V_m = \frac{BkT\left(\text{productLog}\left(\frac{\exp\left(J_o + J_{sc}\right)}{J_o}\right)-1\right)}{q}, \tag{15}$$

where productLog is a function related to a logarithmic solution, e.g., *ProductLog* (z) provides a solution for w in $z = we^w$. Thus, the temperature dependence on the fill factor satisfies

$$\frac{dFF}{dT} = \frac{\left(1-\frac{\exp(qV_m/kT)-1}{\exp(qV_{oc}/kT)-1}\right)V_m'}{V_o} - \frac{\left(1-\frac{\exp(qV_m/kT)-1}{\exp(qV_{oc}/kT)-1}\right)V_m V_{oc}'}{V_{oc}^2} + \frac{V_m \exp(qV_0/kT)\left(-1+\exp(qV_m/kT)\right)\left(qV_{oc}'/kT - qV_{oc}/kT^2\right)}{V_{oc}\left(\exp(qV_{oc}/kT)-1\right)^2} - \frac{V_m \exp(qV_m/kT)\left(qV_m'/kT - qV_m/kT^2\right)}{V_{oc}\exp(qV_{oc}/kT)-1} \quad (16)$$

where $V_m' = \partial V_m/\partial T$ and $V_{oc}' = \partial V_{oc}/\partial T$.

Through these relationships, the temperature dependence of the efficiency can be expressed by formula:

$$\frac{1}{\eta}\frac{\partial \eta}{\partial T} = \frac{1}{V_{oc}}\frac{\partial V_{oc}}{\partial T} + \frac{1}{J_{sc}}\frac{\partial J_{sc}}{\partial T} + \frac{1}{FF}\frac{\partial FF}{\partial T}. \quad (17)$$

3. CONFIRMATION WITH EXPERIMENTAL DATA

In this section, the model proposed is compared with experiment data from [18] and [15]. In the beginning, the model and the experimental results were compared with regard to the relation between temperature to V_{OC} value that has been done by Tobnaghi et al. (2013) using monocrystalline silicon solar cells. Since there is no analytic expression of temperature dependence of J_{SC}, in Fig. 3 we obtain the expression through linear fitting method: J_{SC} = 33.7491 + 0.00083 T and $\partial J_{sc}/\partial T = 0.00083$.

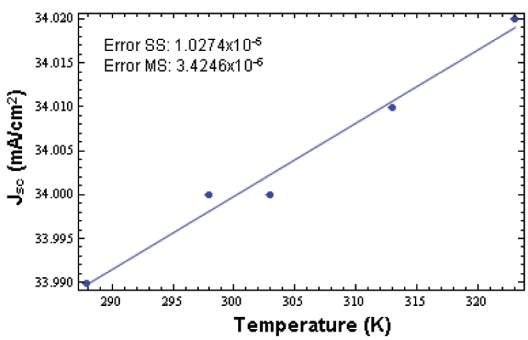

Fig. 3. Linear fitting of the relationship between *Jsc* and the temperature on the solar cell in [18].

The relation between $E_g(0)$, average phonon energy, and electron-phonon coupling parameters of silicon and GaAs are shown in Table 1. The changes in performance parameters: J_{SC}, V_{OC}, V_m, FF, and efficiency are reported in Fig. 4. Using Eq. (10) along with the J_{SC} expression and the bandgap energy parameter data from silicon, the comparison between the model and the experimental results is shown in Fig. 4(a). It is clear that the proposed model, which has the V_{OC} properties inversely proportional to the temperature, is acceptable because the model can provide a small variance and almost similar to all experimental data. This result is also obtained by parameters fitting solar cells in [18], which are $C = 2476.23$ mA cm^{-2} K^3, $A = 0.2145$, and $m = 0.3545$. Thus, it can be stated that the quality of solar cell was low according to its m parameter.

Table 1

Energy Gap Parameters for Si and GaAs [14]

	$E_g(0)$ (eV)	S	$\langle \hbar\omega \rangle$ (meV)
Si	1.170	1.49	25.5
GaAs	1.521	3.00	26.7

The comparison of V_m values as in Eq. (15) with the experimental results is shown in Fig. 4(b). The expression of J_0 is determined by Eq. (9). Through the fitting data obtained value $B = 0.1766$ for solar cells in [18]. Furthermore, in Fig. 4(c) it appears that the expression of the FF formulation in Eq. (13) is sufficient in accordance with the experimental results. The constant values of F and G are 1.924 and 2.304, respectively. It is clear that in the temperature range from 288 K to 323 K the value of FF is inversely proportional to the temperature. Thus, based on these performance parameters, it is clear that the efficiency of the solar cell will also be inversely proportional to the temperature as shown in Fig. 4(d). The efficiency of a solar cell will decrease with increasing temperature. Thus, based on the suitability of all models of solar cell performance parameters on the experimental results it can be stated that the model we proposed has high accuracy to describe the dependence of solar cell performance on temperature changes.

Apart from the above four parameters, we also verify the temperature dependence of *Voc* on the experimental results of Si and GaAs solar cells in [15]. Based on the experimental data in [15], Table 1 and the V_{OC} expression as a function of temperature in Eq. (11) we obtain $\left(1/V_{oc}\right)\left(\partial V_{oc}/\partial T\right) = -0.24\%$ for GaAs solar cells with $V_{OC} = 0.96$ V at 300 K. As for solar cell Si with $V_{OC} = 0.67$ V at 300 K we obtain $\left(1/V_{oc}\right)\left(\partial V_{oc}/\partial T\right) = -0.30\,\%$. Our calculations are very close to the experimental results where the results of $\left(1/V_{oc}\right)\left(\partial V_{oc}/\partial T\right)$ in GaAs solar cell is -0.25 % while for Si solar cell is -0.30 %. In addition, our calculations are more accurate than Fan's (1986) calculations. The difference in results arises from the application of phononic energy correction and the phonon-electron coupling in our calculations.

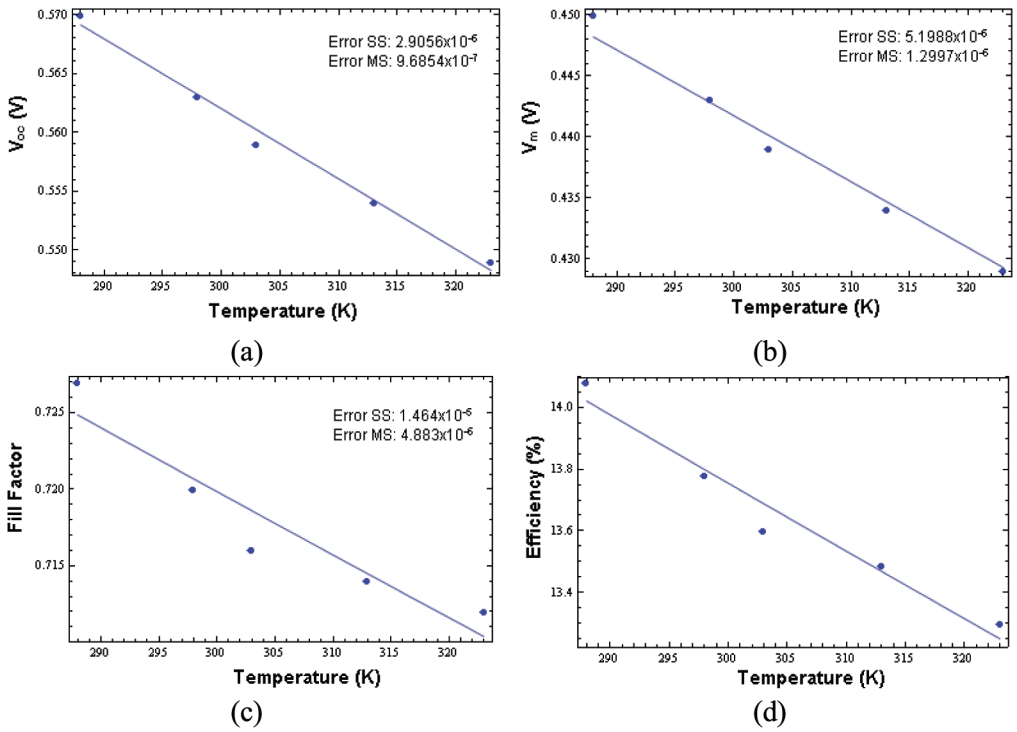

Fig. 4. The values of solar cell performance parameters: (a) V_{OC}, (b) V_m, (c) *FF*, and (d) efficiency as a function of temperature in [18].

4. CONCLUSIONS

Through expression of bandgap relationship with temperature involving, electron-phonon coupling interaction can be shown that the higher temperature will decrease solar cell performance parameters such as: V_{OC}, V_m, *FF*, and the efficiency. The models with the electron-phonon interaction correction are quite accurate. The experimental values of V_{OC}, V_m, *FF*, efficiency and temperature dependence of V_{OC} are almost similar to the proposed model.

ACKNOWLEDGEMENTS

We gratefully acknowledge the funding from USAID through the SHERA programme – Centre for Development of Sustainable Region (CDSR).

REFERENCES

1. Hitha, P., Sosale, S.S., Sushmitha, S., & Rekha, K.R. (2017). Performance analysis of various-4-wheelers with IC engines for hybridization. *International Journal of Advance Research, Ideas, and Innovations in Technology 3*(3), 1322–1327.
2. Chu, S., Cui, Y., & Liu, N. (2017). The path towards sustainable energy. *Nature Materials 16*, 16–22.

3. Ferreira, A., Kunh, S.S., Fagnani, K.C., De Souza, T.A., Tonezer, C., Santos, G.R.D., & Coimbra-Araujo, C.H. (2018). Economic overview of the use and production of photovoltaic solar energy in Brazil. *Renewable and Sustainable Energy Reviews 81*, 181–191.
4. Khemariya, M., Mittal, A., Baredar, P., & Singh, A. (2017). Cost and size optimization of solat photovoltaic and fuel cell based integrated energy system for un-electrified village. *Journal of Energy Storage, 14*, 62–70.
5. Huang, X., Fu, H., Chen, H., Lu, Z., Baranowski, I., Montes, J., Yang, T.H., Gunning, B.P., Koleske, D., & Zhao, Y. (2017). Reliability analysis of InGaN/GaN multi-quantum-well solar cells under thermal stress. *Applied Physics Letters*, *111*, 2333511.
6. Saidan, M., Albaali, A., Alasis, E., & Kaldellis, J. (2016). Experimental study on the effect of dust deposition on solar photovoltaic panels in desert environtment. *Renewable Energy*, *92*, 499–505.
7. Sun, Y., Wu, Y., Fang, X., Xu, L., Ma, Z., Lu, Y., Zhang, W.H., Yu, Q., Yuan, N., & Ding, J. (2017). Long-term stability of organic-inorganic hybrid perovskite solar cells with high efficiency under high humidity conditions. *J. Mater. Chem.*, A 5, 1374–1379.
8. Perl, E.E., Simon, J., Geisz, J.F., Lee, M.J., Friedman, D.J., & Steiner, M.A. (2017). Measurements and modelling of III-V solar cells at high temperatures up to 400°C. *2017 IEEE 44th Photovoltaic Specialist Conference (PVSC)*, 1–14.
9. Singh, P., & Ravindra, N. (2012). Temperature dependence of solar cell performance-an analysis. *Solar Energy Materials & Solar Cells*, *101*, 36–45.
10. Tamrakar, V., Gupta, S., & Sawle, Y. (2015). Single-diode PV cell modeling and study of characteristics of single and two-diode equivalent circuit. *Electrical and Electronics Engineering: An International Journal*, *4*(3), 13–24.
11. Schubert, E. (2006). LED basics: Electrical properties. *Light-Emitting Diodes*. Cambridge: Cambridge University Press.
12. Varshi, Y. (1967). Temperature dependence of the energy gap in semiconductors. *Physics (Utrecht), 34*, 149–154.
13. Cuce, E., Cuce, P.M., Karakas, I.H., & Bali, T. (2017). An accurate model for photovoltaic (PV) modules to determine electrical characteristics and thermodynamic performance parameters. *Energy Conversion and Management*, *146*, 205–216
14. O'Donnell, K., & Chen, X. (1991). Temperature dependence of semiconductor band gaps. *Appl. Phys. Lett. 58*(15), 2924–2926.
15. Fan, F. (1986). Theoretical temperature dependence of solar cell parameters. *Solar Cells, 17*, 309–315.
16. Green, M., Emery, K., Hishikawa, Y., & Warta, W. (2011). Solar cell efficiency tables (version 37). *Progress in Photovoltaics: Research and Applications, 19*, 84–92.
17. Wysocki, J., & Rappaport, P. (1960). Effect of temperature on photovoltaic solar energy conversion. *Journal of Applied Physics, 31*, 571–578.
18. Tobnaghi, D., Madatov, R., & Naderi, D. (2013). The effect of temperature on electrical parameters of solar cells. *International Journal of Advanced Research in Electrical, Electronics and Instrumentation Engineering, 2*(12), 6404–6407.

PRECĪZS MODELIS SAULES ELEMENTU EFEKTIVITĀTES ATKARĪBAI NO TEMPERATŪRAS PĒC FONONA ENERĢIJAS KOREKCIJAS

J. Tiandho, V. Sunanda, F. Afriani, A. Indriavati, T. P. Handajani

K o p s a v i l k u m s

Daudzos eksperimentos tiek ziņots, ka saules elementu efektivitāte samazinās, pieaugot temperatūrai. Šis efekts rodas materiāla iekšējo nesēju koncentrācijas pieauguma dēļ, kas tieši ietekmē atgriezenisko piesātinājuma strāvu (J_0). Rezultātā, tukšgaitas spriegums, kas ir apgriezti proporcionāls J_0, samazinās diezgan strauji, pieaugot temperatūrai. Iekšējā nesēja koncentrācija tiek noteikta, izmantojot materiāla brīvo elektronu enerģiju un tās temperatūru. Varšni attiecība ir saistība starp brīvo elektronu enerģijas izmaiņām un pusvadītāju temperatūru, kas plaši izmantota saules elementu efektivitātes modelī. Tomēr pastāv problēma, jo Varšni attiecība nosaka tikai vibrācijas daļas devumu, un tas attiecas tikai uz temperatūru, kas ir daudz lielāka par Debaja temperatūru. Pētījumos tiek piedāvāts saules elementu efektivitātes temperatūras atkarības modelis, kas ietver fonona enerģijas korekciju un elektronu-fononu mijiedarbību. Šī korekcija tiek piemērota, jo elektronu-fononu sakabes mijiedarbība ir pusvadītāju raksturīgā mijiedarbība. Mijiedarbības esamību nevar izslēgt nedz eksperimentāli, nedz teorētiski. Piedāvātais modelis tiek salīdzināts ar eksperimentāliem datiem, kuriem ir diezgan augsta precizitāte.

29.06.2018.

sciendo

LATVIAN JOURNAL OF PHYSICS
AND TECHNICAL SCIENCES
2018, N 5

DOI: 10.2478/lpts-2018-0033

HEAT COST ALLOCATION IN MULTI-APARTMENT BUILDINGS: A LITERATURE REVIEW

M. Laicāns[1], I. Puķīte [1], I. Geipele[1], N. Zeltins[2,] A. Greķis[1]

[1]Riga Technical University,
Institute of Civil Engineering and Real Estate Economics,
6-210 Kalnciema Str. , Riga, LV-1048, LATVIA
E-mail: iveta.pukite@rtu.lv
[2]Institute of Physical Energetics
11 Krivu Str., Riga, LV-1006, LATVIA

Literature review aims at examining various scientific articles on the accounting methods of individual heat consumption and heat cost allocation.

Nowadays, accounting methods of heat consumption and heat cost allocation in multi-apartment buildings are a topical issue. Heat and water supply is one of the key services provided to residential buildings and their residents. Residents appreciate solutions that allow them consume as much heat as they need and are able to pay, but on condition that the calculation methodology is understandable and easy to perceive.

Directive 2010/31/EU on the Energy Performance of Buildings adopted by the European Parliament and the Council (Directive 2010/31/EU of the European Parliament and of the Council, 2010) stipulates that owners or tenants of buildings shall be provided with the information on energy efficiency measures, their goals and objectives, cost effective ways to improve the energy performance of a particular building and, where appropriate, in the case of available financial instruments to improve the energy performance of a particular building.

The aim of the research is to perform literature analysis using topical articles on the accounting methods of individual heat consumption and heat cost allocation, which are published in the Web of Science and Scopus scientific databases, by analysing and comparing the published results.

Keywords: *distribution of heat consumption, heat cost allocators, heat energy accounting, individual heat metering*

1. INTRODUCTION

Directive 2012/27/EU of the European Parliament and of the Council (EPC) stipulates that “In multi-apartment and multi-purpose buildings with a central heat-

ing/cooling source or supplied from a district heating network or from a central source serving multiple buildings, individual consumption meters shall also be installed by 31 December 2016 to measure the consumption of heat or cooling or hot water for each unit where technically feasible and cost-efficient. Where the use of individual meters is not technically feasible or not cost-efficient, to measure heating, individual heat cost allocators shall be used for measuring heat consumption at each radiator, unless it is shown by the Member State in question that the installation of such heat cost allocators would not be cost-efficient. In those cases, alternative cost-efficient methods of heat consumption measurement may be considered." (EPC Directive 2012/27/EU, 2012).

Several studies refer to EPC Directive 2012/27/EU on the Energy Performance of Buildings (EPC 2012/27/EU, 2012), which seeks to ensure, to the extent technically feasible, cost-efficient and proportionate to the potential energy savings, that end users of central heating and of domestic hot water at a competitive cost would be provided with individual meters that accurately measure the actual energy consumption of the end user and provide information on actual usage time, envisaging bills free-of-charge that would promote the efficient use of heat and increase consumption efficiency in the sector of residential buildings by mentioning heat meters as effective tools to increase energy efficiency without compromising comfort and setting mandatory installation of such devices by 31 December 2016 in all multi-apartment buildings with a central heating system (Celenza, 2015) (Grasmanis, 2015), (Siggelsten, 2013), (Siggelsten, 2014), (Wang, 2015). In publications, one option is to install energy meters on the radiator surface to measure the amount of consumed heat, which is supplied to the apartment (Cholewa, 2015). In Italy, a number of laws confirm the mandatory installation of temperature control and heat energy measurement systems in significantly renovated buildings, and in new buildings they must be installed in each flat without exception (Celenza, 2015), as well as the laws determine the maximum allowable error in heat distribution systems and devices, which must not exceed ± 5 % (Ficco, 2016).

Residents of multi-apartment buildings have different comfort temperatures; therefore, it should be noted that there is a possibility to regulate heat supply to their apartments during the heating season, thus also paying according to their needs and possibilities, where the main criterion is not the heated area, but the actually consumed amount of energy.

The aim of the research is to perform a literature analysis of the accounting methods of individual heat consumption and heat cost allocation. Within the framework of the research, the authors analyse various scientific articles, by clarifying the opinions of scientists and evaluating research results.

To achieve the aim of the research, the following tasks have been set: 1) to select and analyse scientific articles on the subject under study; 2) to identify the main indicators characterising heat cost calculation and allocation in multi-apartment residential buildings; 3) to find out calculation methods of heat consumption; 4) to determine the role of heat cost calculation and allocation in multi-apartment residential buildings; 5) to draw conclusions.

The subject of the research is heat cost allocation, the object of the research – multi-apartment residential buildings.

In the course of literature analysis, the authors have used topical articles of the Web of Science and Scopus scientific databases, which were published in the period from 2006 to 2016.

2. HEAT ENERGY ACCOUNTING AND DISTRIBUTION

The heat consumption accounting system at the building level records the total heat consumption in the building, and the heat cost allocation method is used to divide the total cost of heat among the apartments. Finnish researchers point out that due to the fact that the indoor temperatures of the multi-apartment buildings are generally not equal, static heat transfer between apartments cannot be avoided. Therefore, in order to measure the fair heat consumption of each apartment, the charging system should be able to determine the static heat transfer, preferably without the real measurement method (Pakanen, 2006).

An individual measuring method in multi-apartment buildings often focuses on the consumption of heat in one room or a group of premises (in an apartment). The principle of the method is that meters determine how the overall heat energy costs are divided between the flats, and these systems are called heat cost allocation systems. In some countries, the system for determining the individual heat consumption has been strengthened by law. The European Commission (EC) recommends that all Member States apply this principle. This regulation has created a range of technical solutions and a set of commercial measuring products (Celenza, 2015), (Liu, 2012).

The heat cost distributor or allocator is an electronic device that determines the proportionality of the heat produced by each radiator in the apartment. These allocators can be installed practically on all types of radiators, both steel panel and sectional radiators. They can be applied to both single-pipe and dual-pipe systems. Heat cost calculation is performed by dividing the total heat costs by allocator measurements. Remote data collection systems are used for data collection and compilation.

Apart from the differences in technical solutions, there are various ways as how to address energy transfer between different apartments or premises with the subsequent cost sharing. Some fee-sharing systems use specific factors to adjust the cost of the calculation period, which is most often one calendar month, according to the location of the apartment in the building, while other methods use project data on static heat transfer to determine heat transfer between apartments. However, all currently available methods only produce rough results, and this problem is known to heat consumers. Finnish researchers clearly indicate that a heat consumption measurement system that collects only consumption data cannot provide a quick and easy way to determine the real heat transfer between apartments and cannot evaluate information about materials, furniture, period and frequency of residence, and the amount of internal heat in each apartment, specifying that the ventilation differs in each apartment depending on the air leakage and the location of the apartment (Pakanen, 2006).

The research concludes that the calculation of heat consumption costs using incomplete information will lead to significant calculation errors. If heating costs

are not adjusted to each apartment individually, the results of the cost calculation method may approach the model according to which residents pay a steady fee for heating an apartment based on the energy consumption per square metre that does not encourage citizens to take any initiatives to reduce the demand for heating in the apartment and residents can just reduce the room temperature by opening windows or doors (Kavgic, 2012).

3. DISCUSSION AND RESULTS

Heating bills issued by heat energy suppliers to residents of multi-apartment residential buildings are based on the readings of heat meters. The boundary of the regulated public service is the introduction of the heat pipe in the building where the heat meter is located, according to which the amount of heat supplied is determined and the payments for the heat energy supplied to the whole building are settled (EUR/MWh). Further calculations are carried out by the manager of a multi-apartment residential building, by dividing the fee for the heat energy supplied, thus forming a charge for heating the area of 1 m^2.

Individual heat accounting (heating and hot water) is a very important tool for promoting the use of heat energy in multi-apartment residential buildings with a central heating system. The detailed availability of heat consumption data increases the ability of consumers to identify inefficient energy consumption and make their consumption strategy more dynamic (Celenza, 2015).

An assessment of the distribution of heat energy between engineering systems is of importance in multi-apartment residential buildings with the required heat energy consumption for heating, hot water heating and circulation purposes. The heat consumption required for the heating of hot water is determined constant throughout the year. In multi-apartment residential buildings, the amount of heat required for hot water heating purposes could be about 25 % of the total annual consumption of heat energy (or 20 to 25 kWh/m^2 per year) for multi-apartment residential buildings with low thermal resistance, which increases in buildings with higher heat resistance. According to the research data, in multi-apartment buildings in Riga, one person consumes 41 liters of hot water at a temperature of + 50–55 ^oC per day (Grasmanis, 2013).

Another study, based on measurements from 182 Finnish apartments with 379 residents, confirms that the average consumption of hot water is 43 liters per person per day (see Fig. 1.1) in apartments without individual hot water meters and 35 liters per person per day with individual hot water meters in apartments (Ahmed, 2015).

Chinese researchers Liu et al. refer to the methods already used in the country and only this study uses the calculation methods of heat consumption (see Fig. 1), which are not used in the country but have been successfully adopted in Europe and used in many European countries.

Ziemele et al. propose an algorithm for determining the cost of heat consumption in multi-apartment residential buildings (see Fig. 2). The study indicates that, first of all, the total heat energy consumption in a multi-apartment residential building is specified in Module 1. Second, in the modeling process of calculation it is

necessary to obtain the total amount of heat consumed for heating purposes (Module 2). Each apartment needs different amount of heat in order to ensure comfort conditions; therefore, it is necessary to introduce additional criteria for the assessment of heat consumption in order to prevent the unfair allocation of heat costs. These criteria are taken into account in Module 3, using certain assumptions (Module 4), determining the heat cost for each apartment in accordance with the method of heat cost allocation (Ziemele, 2015).

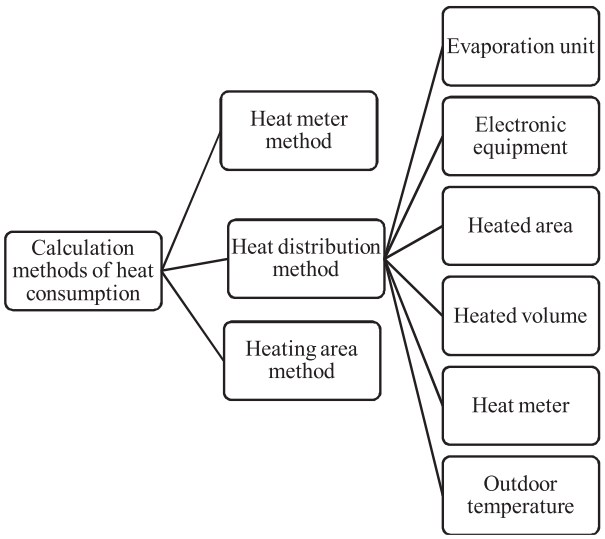

Fig. 1. Calculation methods of heat energy consumption in China (Liu, 2012).

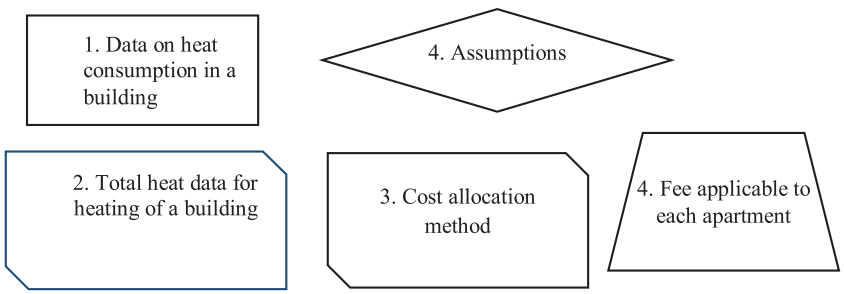

Fig. 2. Calculation of fee for heat energy consumed (Ziemele, 2015).

Studies in Germany have shown a 10 %–40 % decrease in heat consumption if the apartments are equipped with individual heat meters. The need to introduce individual energy and other resource meters can be observed since the 1920s, when central heating systems began to be used in major European cities. Kupler, for the first time in his studies, mentioned the existence of such meters in 1929. Liu points out that the calculation of heat cost allocation is mainly based on a heated area with two main types of heat consumption billing options – basic consumption at the level

of the entire building and consumption at the apartment level, concluding that heating costs in Europe are calculated at two stages: the total heat consumption of the building and consumption of each apartment as it is in Germany. Insulated buildings with mechanical ventilation and the ability to control indoor temperatures in Finland make energy savings economically less advantageous compared to investments by installing individual heat meters (Liu, 2015).

Calculating heating costs by applying the average room temperature or temperature of a group of premises in each household, the initial financial contribution and regular management costs are the same as the installation of heat distributors (allocators), only in case of average temperature consumers would be able to open the windows by deliberately lowering heating costs and the goal of the efficient use of heat would not be achieved, as a result of which this method is prohibited in Germany (Liu, 2015).

The individual heat meter determines heat consumption by calculating the circulation rate of heat flow and the difference between the temperatures of inward flow and outward flow (see Fig. 1.4), thus an overall uncertainty in the estimation of heat consumption can be around 2.9 %–8.9 %. In most cases, manufacturers specify an uncertainty of the heat meter of 4.4 % (Celenza, 2015).

Heat meters measure heat consumption over a certain period of time, multiplying by the temperature difference of the heat carrier, entering the closed apartment heating system and escaping from the heating system of the apartment. Heat meters consist of a flow sensor (V), a pair of temperature sensors (Tie, Tiz) and a calculator with a built-in processor and software for measuring heat consumption (Ficco, 2016).

An individual heat meter installed near the radiator can measure the amount of heat supplied to the apartment, but if there is more than one radiator in the apartment, this can be a very economically ineffective method and as an alternative a heat meter is installed on each radiator; however, the study clearly demonstrates errors in both methods in the case of an apartment building with a centralised mechanical ventilation system with a heat recovery function (Siggelsten, 2013).

For individual heat consumption accounting, heat cost allocators can be used in heating systems that are supplied with heaters, and heat cost dividers (alcocators) are installed on each heat source unit together with a thermostatic valve, and studies performed demonstrate an overall uncertainty of an average of 9.2 %. Rarely, uncertainty of allocators is less than 3.5 % and at worst, it can reach 40.5 % (Celenza, 2015).

Individual heat cost allocators are not measuring equipment and do not actually show actual heat consumption in a particular apartment, but refer to separate calculation procedures designed to allocate energy costs between different apartments in multi-apartment buildings with central heating (Cholewa, 2015).

The individual heat metering method with allocators is mostly applied to dwellings in Europe (Finland, Germany, Austria etc.) (Huebner, 2013), because in these countries the thermal insulation properties of building envelopes are generally good; hence, the difference in the heating fee caused by different locations of apartments in the building has less impact on the amount of the fee and the heating costs

in general for the apartment make up a small percentage of the total income of the person, so the difference in the heeting fee is insignificant. The total cost of heating, including both heating and hot water, accounts for only 2 %–5 % of the total income of the population in the developed countries (Liu, 2015).

Electronic individual heat cost allocators can effectively control the opening of windows as they also measure room temperature and their accuracy is higher than that of evaporative heat cost allocators, but also costs are higher. It should also be noted that electronic meters can only be installed on certain types of radiators, the availability of installation is similar to evaporators, and the quality depends on the installation and accuracy of the calculation algorithm (Liu, 2015).

The method of measurement with heat cost allocators should also take into account the heat loss through the building envelope and heat gain, the heat flow from the riser pipes; it is necessary to recalculate the radiator assessment factor and the heat transfer between the apartments, as well as the fixed and variable proportion of the heat content each month, while the fixed consumption consists of the heat gain from uncovered heating network pipes in apartments and heat consumption in common areas (Ziemele, 2015).

The heat cost allocation method, which relatively solves the problem of heat transfer between adjacent apartments, determines the value of the temperature of each thermostat that is sent to a central processor, which theoretically means that the residents pay for the desired indoor temperature and it does not matter whether the heat comes from radiators or from adjacent apartments, but researchers point to the negative aspects of this method, because this method ignores the effect of window opening as well as the factor of solar radiation and internal heat gain (Fabi, 2012).

As an alternative to the above-mentioned methods, Liu et al. recommend an "on-off" method based on the operating time ratio of the thermostat valve, which will not require any correction in terms of the location of an apartment, because the heating system must be provided with heaters according to the location of an apartment in the multi-apartment residential building – the more exterior walls in the apartment, the larger radiators; however, this method does not take into account the heat transfer between adjacent apartments and the effect of the ventilation system on the total heat energy consumption balance (Liu, 2012).

In his research, Siggelsten mentions several studies that found out that the heat transfer between adjacent apartments could lead to an unfair distribution of heat costs and, in his research, he provides an example of unfair heat cost allocation in an existing multi-apartment building, for example, in an apartment of the building with almost no heat cost allocators during the heating season, which is impossible in Swedish climatic conditions. The research also indicates that 6 out of 16 apartments are overcharged and 7 out of 16 apartments pay less; therefore, in his research, he proposes making adjustments to the measurements provided by heat cost allocators, by comparing internal heat gain with the electricity consumption in an apartment, but he notes that such a calculation method only complicates the acquisition of data for the calculation model (Siggelsten, 2014).

Multi-apartment residential buildings comprise a significant sector of the heat energy market as the recipient of services and the end consumer. Consequently, by

introducing individual heat cost allocators in separate apartments, it is possible to reduce the total heat energy consumption of a residential building. In order to achieve this goal, it is necessary to introduce a fair calculation of the heat cost allocation, taking into account the various methods used in practice and the correction coefficients.

4. CONCLUSIONS

1. Latvian researchers note that different results of hot water consumption provided in various studies can be explained by the temperature of hot water that differs in the collection point, in the case of higher temperatures, hot water consumption will be lower. Studies confirm that hot water consumption is not attributed to the behaviour and habits of residents of multi-apartment residential building.
2. Heat energy losses with hot water circulation lines in multi-apartment residential building are significant, and heat energy consumption with a high degree of precision can be calculated in the summer. In the heating period, correction is not applied to calculations of losses with hot water circulation lines in the summer. However, to determine the fee for the heat energy necessary for the circulation of hot water, several calculation methods are used, where the cost of heat energy consumption is divided by: the area of the apartment (MWh/m^2); number of apartments (MWh/flat); number of residents (MWh/person).
3. Accurate measurement of individual heat consumption is a complicated process because the energy consumed by the upper corner apartments is two to three times higher than the energy consumed by apartments located in another part of the building and, besides, heating costs can increase by 20 %–30 % if the adjacent apartments are not heated and it is considered that the existing measurement methods cannot effectively solve these two problems, so they are not relevant.
4. The installation of heat cost allocators is not classified as a method for reducing energy consumption, but it allows heat consumers to freely choose the desired comfort indoor temperature for which they are willing to pay. Therefore, it is very difficult to accurately calculate the economic benefits of installing heat cost allocators, since it is not possible to accurately predict heat savings.
5. Researchers indicate that the introduction of heat cost allocation is a tool that can be used to ensure that the consumers pay only for the heat supplied to them and that every resident can follow the heat consumption and this increases the motivation of the population to regulate the indoor temperature by reducing the heat consumption, but in this case the heat gain from uncovered heat riser pipes in apartments varies from 22.5 % to 4.1 %.

REFERENCES

1. Ahmed, K., Pylsy, P., & Kurnitski, J. (2015). Monthly domestic hot water profiles for energy calculation in Finnish apartment buildings. *Energy and Buildings*, *97*, 77–85.
2. Celenza, L., Dell'Isola, M., Ficco, G., Palella, B.I., & Riccio, G. (2015). Heat accounting in historical buildings. *Energy and Buildings, 95*, 47–56.

3. Cholewa, T., & Siuta-Olcha, A. (2015). Long term experimental evaluation of the influence of heat cost allocators on energy consumption in a multifamily building. *Energy and Buildings*, *104*, 122–130.
4. EPC Directive 2010/31/EU. Directive of the European Parliament and of the Council. On the Energy Performance of Buildings. [Online] 19 May 2010. [Accessed: 10 March 2017] http://eurlex.europa.eu/LexUriServ/LexUriServ.do?uri=OJ:L:2010:153:0013:0035:lv:PDF.
5. EPC Directive 2012/27/EU. Directive of the European Parliament and of the Council. On the Energy Performance of Buildings. [Online] 25 October 2012. [Accessed: 12 March 2017] http://eurlex.europa.eu/LexUriServ/LexUriServ.do?uri=OJ:L:2012:315:0001:0056:LV:PD.
6. Fabi, V., Andersen, R.V., Corgnati, S., & Olesen, B.W. (2015). Occupants' window opening behaviour: A literature review of factors influencing occupant behaviour and models. *Building and Environment*, *58*, 188–198.
7. Ficco, G., Celenza, L., Dell'Isola, M., & Vigo, P. (2016). Experimental comparison of residential heat accounting systems at critical conditions. *Energy and Buildings*, *130*, 477–487.
8. Grasmanis, D., Greķis, A., & Talcis, N. (2013). Heat consumption assessment of the domestic hot water systems in the apartment buildings. *Construction Science*, *14*, 38–43.
9. Grasmanis, D., Talcis, N., & Greķis, A. (2015). Buildings, Heat Consumption Assessment of the Domestic Hot Water Systems in the Apartment. *Construction Science*, 167–176.
10. Huebner, G.M., Cooper, J., & Jones, K. (2013). Domestic energy consumption – What role do comfort, habit, and knowledge about the heating system play? *Energy and Buildings*, *66*, 626–636.
11. Kavgic, M., Summerfield, A., Mumovic, D., Stevanovic, Z.M., Turanjanin, V., & Stevanovic, Z.Z. (2012). Characteristics of indoor temperatures over winter for Belgrade urban dwellings: Indications of thermal comfort and space heating energy demand. *Energy and Buildings*, *47*, 506–514.
12. Liu, L. (2015). Major issues and solutions in the management system of space heating system in North China. *Renewable and Sustainable Energy Reviews*, *130*, 221–231.
13. Liu, L., Fu, L., & Jiang, Y. (2012). A new "wireless on-off control" technique for adjusting and metering household heat in district heating system. *Applied Thermal Engineering*, *36*, 202–209.
14. Pakanen, J., & Karjalainen, S. (2006). Estimating static heat flows in buildings for energy allocation systems. *Energy and Buildings*, *38*(9), 1044–1052.
15. Siggelsten, S. (2014). Reallocation of heating costs due to heat transfer between adjacent apartaments. *Energy and Buildings*, *75*, 256–263.
16. Siggelsten, S., & Olander, S. (2013). Individual metering and charging of heat and hot water in Swedish housing cooperatives. *Energy Policy*, *61*, 874–880.
17. Wang, J., & Li, D. (2015). Economic and technical analysis of several heat metering modes: A case study from Beijing, China. *Procedia Engineering*, *121*, 1037–1043.
18. Ziemele, J., Pakere, I., Blumberga, D., & Zogla, G. (2015). Economy of heat cost allocation in apartment buildings. *Energy Procedia*, *72*, 87–94.

SILTUMA MAKSU SADALĪŠANA DAUDZDZĪVOKĻU MĀJĀS

M. Laicāns, I. Puķīte, I. Geipele, N. Zeltiņš, A. Greķis

K o p s a v i l k u m s

Lieteratūras apskatā tiks izvērtēti dažādi zinātniski raksti par individuālās siltumenerģijas patēriņa uzskaites un maksas daļas noteikšanas metodēm.

Mūsdienās siltumenerģijas patēriņa uzskaites un maksas daļas noteikšanas metodes daudzdzīvokļu ēkās ir aktuāla problēma. Siltuma un ūdens nodrošināšana ir viens no pamatpakalpojumiem, kas tiek nodorošināts dzīvojamām mājām un tajos dzīvojošām personām. Iedzīvotāji augsti novērtē risinājumus, kas ļauj siltumenerģiju patērēt tik, cik katrs vēlas un spēj apmaksāt, bet ar nosacījumu, ka aprēķina metodika ir saprotama un viegli uztverama.

EPP direktīva 2010/31/ES par ēku energoefektivitāti, nosaka sniegt informāciju ēku īpašniekiem vai īrniekiem par energoefektivitātes pasākumiem, to nolūkiem un mērķiem, par rentabliem veidiem, kā uzlabot attiecīgo ēku energoefektivitāti un, vajadzības gadījumā, par pieejamiem finanšu instrumentiem, lai uzlabotu attiecīgās ēkas energoefektivitāti.

Pētījuma mērķis ir veikt literatūras analīzi par individuālās siltumenerģijas patēriņa uzskaites un maksas daļas noteikšanas metodēm. Pētījuma priekšmets ir siltuma maksas sadalīšana, pētījuma objekts – daudzdzīvokļu dzīvojamās mājas.

Literatūras analīzes gaitā tika izmantoti aktuālie raksti zinātniskajās datubāzēs Web of Science un Scopus, kuri ir publicēti laika posmā no 2006.gada īdz 2016. gadam.

18.07.2018.

sciendo

LATVIAN JOURNAL OF PHYSICS
AND TECHNICAL SCIENCES
2018, N 5

DOI: 10.2478/lpts-2018-0034

SOLID STATE PHYSICS

FIRST-PRINCIPLES MODELLING OF N-DOPED Co_3O_4

G.A. Kaptagay[1], Yu.A. Mastrikov[2], E.A. Kotomin[2]

[1] Kazakh State Women's Teacher Training University, Almaty, Kazakhstan
[2] Institute of Solid State Physics, University of Latvia

N-doped Co_3O_4 is a promising electrocatalyst. By means of first-principles calculations, various concentrations and spatial arrangements of N_O atoms were modelled. Mutual interaction of the dopant atoms was analysed with respect to single N_O atom. Charge redistribution, caused by doping, was calculated.

Keywords: Co_3O_4, OER, electrocatalyst

1. INTRODUCTION

Oxygen Evolution Reaction (OER) is the essential process for many rapidly developing applications, such as energy conversion and storage [1]. Water splitting devices, some types of fuel cells as well as rechargeable batteries require an effective OER electrocatalyst. Performance of the catalyst depends on overpotential. Noble metal oxides RuO_2 and IrO_2 with low overpotential demonstrate high performance [2]. The cost of these materials, however, limits their usage. Relatively low overpotential of Co_3O_4 makes it a low-cost alternative of noble metal-based catalysts for OER [3], [4].

Numerous works show that overpotential of oxide catalyst can be reduced by doping [5]–[7]. Our earlier investigation confirms that doping Co_3O_4 by fluorine reduces overpotential, resulting in enhancement of catalytic activity [8]. Recent experimental study [9] demonstrates that doping Co_3O_4 by nitrogen, in the combination with oxygen vacancies, reduces overpotential, improving the overall electrocatalytic activity for OER.

Modelling of the surface reactions requires a preliminary study on the N-doped Co_3O_4 bulk. Analysing interaction energies of N atoms in Co_3O_4, we predict the most favourable spatial arrangement patterns for the dopant. Calculated electron charge redistribution reveals in detail the interaction between nitrogen atoms and Co_3O_4.

2. METHOD AND MODEL

Calculations were performed using the DFT method [10], as implemented in the computer code VASP 5.4 [11]. Applicability of the method to the system under study was already tested [8]. Core electrons were substituted by the US potentials with the PAW method [12] applied.

Table 1

US PAW Potentials of Co and O

Element	Free electrons	E_{cutoff}, eV
Co	$4s^1 3d^8$	267.968
O	$2s^2 2p^4$	400.000
N	$2s^2 2p^3$	400.000

Exchange-correlation was described by the PBE functional [13]. The Hubbard correction U-J=3eV [14] was applied to d-electrons of Co_{tet} as well as Co_{oct} atoms. Spin polarization was implemented in the AAF order, alternating on the Co_{tet} planes. For defects modelling cubic 56-atom supercell model was used. Brillouine zone [15] was sampled with the 2x2x2 Monkhorst-Pack [16] scheme. Plain-waive basis set has the kinetic energy cut-off of 550eV. Charge redistribution was analysed by the Bader method [17], as implemented by Henkelmann et al. [18], [19].

Co_3O_4 has a structure of normal spinel, symmetry group 227 [20]. The tetragonal 8*a* sites are occupied by Co^{2+}, and the octahedral 16*d* sites by Co^{3+}. O^{2-} ions occupy 32*e* sites.

Doping by nitrogen was performed by substitution of oxygen atoms. Four concentrations were tested – 1, 2, 4 and 8 N per 32(O+N) atoms. There are five non-equivalent distances between 32 *e* sites in the supercell – 1–4 and 6NN (32*e*-32*e*). Some coordination spheres are split to the sub-spheres with a small deviation in distances as shown in Fig. 1.

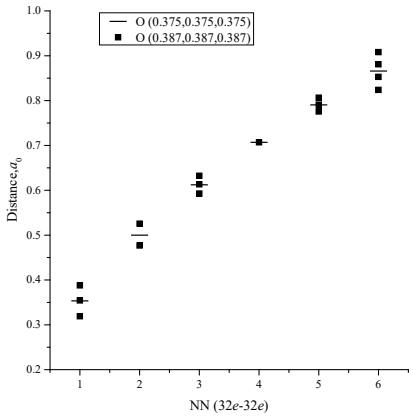

Fig. 1. Nearest neighbours of 32*e*-32*e* sites of Co_3O_4 structure, symmetry group 227.

Two N atoms were placed at each sub-sphere of the 1NN coordination sphere. For the 2NN single calculation was performed at the distance of the first sub-sphere. Two N atoms were also placed at the largest possible distance within the model supercell – 6NN, first subsphere. Four N atoms were arranged in three different configurations, as shown in Table 2.

Table 2

12.5% N Concentration Configurations. Distances between N_O in NN (32*e*-32*e*)

Conf.1	N_O	N_O	N_O	N_O
N_O	0	6	4	2
N_O		0	2	4
N_O			0	6
N_O				0

Conf.2	N_O	N_O	N_O	N_O
N_O	0	1	4	1
N_O		0	1	4
N_O			0	1
N_O				0

Conf.3	N_O	N_O	N_O	N_O
N_O	0	4	4	4
N_O		0	4	4
N_O			0	4
N_O				0

Nanorod was created, by placing N atoms in line, along the [110]. All N atoms in the same line are the 1NN. The smallest distance between the parallel rods is 3NN (Table 3).

Table 3

25% N Concentration Configurations. Distances between N_O in NN (32*e*-32*e*)

	N_O	N_O	N_O	N_O	N_O	N_O	N_O	N_O
N_O	0	1	4	1	4	3	3	4
N_O		0	1	4	3	4	4	3
N_O			0	1	4	3	3	4
N_O				0	3	4	4	3
N_O					0	1	1	4
N_O						0	4	1
N_O							0	1
N_O								0

3. RESULTS

Two N_O atoms, placed at various distances, exhibited predominantly repulsive interaction, except for the smallest possible distance (-0.02eV). The absolute energy values, however, do not exceed 0.1 eV, which characterises the N_O-N_O interaction in Co_3O_4 as neutral (Fig. 2).

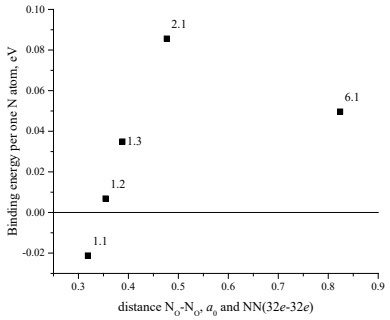

Fig. 2. Binding energy between two N_O doping atoms in Co_3O_4, per N_O atom, depending on the distance.

The N_O-N_O interaction at higher concentrations strongly depends on a particular configuration of the doping atoms (Fig. 3). The lowest energy of -0.03eV corresponds (Conf. 2, Table 2) to a high number of the N_O-N_O 1NN. The most uniform distribution of N_O (Conf. 3 Table 2) gives intermediate repulsion energy of 0.09 eV. The highest binding energy of three calculated configurations of 0.125% is 0.12eV, which can be explained by the presence of the N_O-N_O 2NN bonds (Conf. 1 Table 2) with relatively strong repulsion (Fig. 1).

Aligned in line (Table 3), N_O atoms create stable nano-chains with the binding energy of 0.02eV per atom. Obviously, in such a configuration the primary interaction occurs between the 1NN.

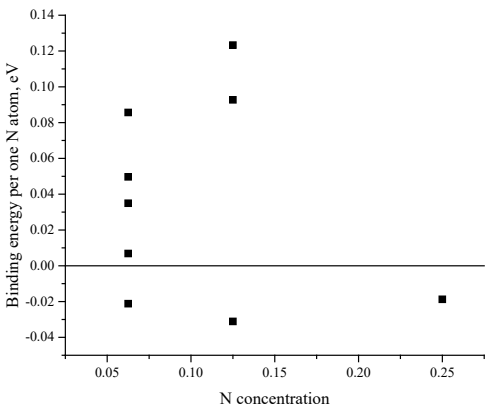

Fig. 3. Binding energy between N_O doping atoms in Co_3O_4, per N_O atom.

Electron charge redistribution, in comparison with undoped Co_3O_4, is localised on the nearest to the dopant Co cations. With respect to oxygen anion, nitrogen anion in Co_3O_4 is less negative. Therefore, Co cations become less positive. Configurations with the lowest binding energy values demonstrate relatively high charge transfer (-0.05 *e*) from the N_O-N_O 1NN pairs to the nearest Co_{tet} - Table 4 (N 1.1NN, Table 2 Conf.2, Table 3 Conf.). For the configuration with the strongest repulsion between N_O-N_O (N 2.1NN), the largest charge value -0.07 *e* was observed on Co_{oct}.

Table 4

Electron Charge Redistribution on Co_{tet} and Co_{oct} Cations in *e*, with respect to the Pure Co_3O_4. Multiplicity of Co cations is given per N_O atom.

single N		
mult.	N	0.02
1	Co_{tet}	-0.02
3	Co_{oct}	-0.02

N 1.1NN		
mult.	N	0.03
1	Co_{oct}	-0.05
1	Co_{oct}	-0.02

N 1.2NN		
mult.	N	0.03
1	Co_{tet}	-0.02
1	Co_{oct}	-0.02
1	Co_{oct}	-0.02
0.5	Co_{oct}	-0.03

N 1.3NN		
mult.	N	0.02
2	Co_{oct}	-0.02
1	Co_{oct}	-0.02

N 2.1NN		
mult	N	0.03
2	Co_{oct}	-0.02
0.5	Co_{oct}	-0.07

N 6.1NN		
mult.	N	0.02
1	Co_{tet}	-0.02
3	Co_{oct}	-0.02

Table 2, Conf.1		
mult.	N	0.03
0	Co_{tet}	
2	Co_{oct}	-0.03
0.5	Co_{oct}	-0.05

Table 2, Conf.2		
mult.	N	0.02
0.5	Co_{tet}	-0.06
1	Co_{oct}	-0.01
1	Co_{oct}	-0.03

Table 2, Conf.3		
mult	N	0.03
1	Co_{tet}	-0.03
3	Co_{oct}	-0.03

Table 3. Conf.		
mult.	N	0.03
0.5	Co_{tet}	-0.06
1	Co_{oct}	-0.04
1	Co_{oct}	-0.02

4. CONCLUSIONS

Small differences (<0.15eV) in interaction energies between various spatial arrangements indicate that in Co_3O_4 oxygen is easily substituted by nitrogen and at room temperature N atoms can be distributed in the material randomly. Repulsive interaction (<0.13eV) between the dopant atoms has been observed for most concentrations and configurations of N_O in Co_3O_4, except for the 1NN. All structures with dominating 1NN interaction, consistently exhibited energetic stability (-0.02-0.03eV), in contrast to other configurations. Binding between two nearest N_O cations is facilitated by an intense electron charge exchange (0.05*e*) with the nearest to both dopant atoms Co_{tet}. Depending on a particular configuration, high charge transfer (>0.05*e*) may show both Co_{tet} and Co_{oct} atoms. The performed calculations create a solid base for the further modelling of OER on N-doped Co_3O_4 surface.

ACKNOWLEDGEMENTS

The project Nr. AP05131211 "First Principles Investigation on Catalytic Properties of N-doped Co_3O_4" is supported by the Ministry of Education and Science of the Republic of Kazakhstan within the framework of the grant funding for scientific and (or) scientific and technical research for 2018-2020. The authors thank T. Inerbaev and A. Popov for fruitful discussions and valuable suggestions. Yu.M. thanks M.Putnina for the technical assistance in preparation of the manuscript.

REFERENCES

1. Cook, T., Dogutan, D., Reece, S., Surendranath, Y., Teets, T., & Nocera, D. (2010). Solar energy supply and storage for the legacy and nonlegacy worlds. *Chemical Reviews, 110*(11), 6474–6502.
2. Reier, T., Oezaslan, M., & Strasser, P. (2012). Electrocatalytic oxygen evolution reaction (OER) on Ru, Ir, and Pt catalysts: A comparative study of nanoparticles and bulk materials. *ACS Catalysis, 2*(8), 1765–1772.
3. Zasada, F., Piskorz, W., Cristol, S., Paul, J.-F., Kotarba, A., & Sojka, Z. (2010). Periodic density functional theory and atomistic thermodynamic studies of cobalt spinel nanocrystals in wet environment: Molecular interpretation of water adsorption equilibria. *The Journal of Physical Chemistry C, 114*(50), 22245–22253.
4. Chen, J., & Selloni, A. (2012). Water adsorption and oxidation at the Co_3O_4 (110) surface. *The Journal of Physical Chemistry Letters, 3*(19), 2808–2814.
5. Liao, P., Keith, J., & Carter, E. (2012). Water oxidation on pure and doped hematite (0001) surfaces: Prediction of Co and Ni as effective dopants for electrocatalysis. *Journal of the American Chemical Society, 134*(32), 13296–13309.
6. Ohnishi, C., Asano, K., Iwamoto, S., Chikama, K., & Inoue, M. (2007). Alkali-doped Co_3O_4 catalysts for direct decomposition of N_2O in the presence of oxygen. *Catalysis Today, 120*(2), 145–150.
7. García-Mota, M., Vojvodic, A., Metiu, H., Man, I., Su, H.-Y., Rossmeisl, J., & Nørskov, J. (2011). Tailoring the activity for oxygen evolution electrocatalysis on rutile TiO_2(110) by transition-metal substitution. *ChemCatChem, 3*(10), 1607–1611.
8. Kaptagay, G., Inerbaev, T., Mastrikov, Y., Kotomin, E., & Akilbekov, A. (2015). Water interaction with perfect and fluorine-doped Co_3O_4 (100) surface. *Solid State Ionics, 277*, 77–82.
9. Xu, L., Wang, Z., Wang, J., Xiao, Z., Huang, X., Liu, Z., & Wang, S. (2017). N-doped nanoporous Co_3O_4 nanosheets with oxygen vacancies as oxygen evolving electrocatalysts. *Nanotechnology, 28*(16), 165402.
10. Kohn, W., & Sham, L. (1965). Self-consistent equations including exchange and correlation effects. *Physical Review, 140*(4A), A1133–A1138.
11. Kresse, G., & Furthmüller, J. (1996). Efficient iterative schemes for *ab initio* total-energy calculations using a plane-wave basis set. *Physical Review B, 54*(16), 11169–11186.
12. Blöchl, P. (1994). Projector augmented-wave method. *Physical Review B, 50*(24), 17953–17979.
13. Perdew, J., Burke, K., & Ernzerhof, M. (1996). Generalized gradient approximation made simple. *Physical Review Letters, 77*(18), 3865–3868.

14. Dudarev, S., Botton, G., Savrasov, S., Humphreys, C., & Sutton, A. (1998). Electron-energy-loss spectra and the structural stability of nickel oxide: An LSDA+U study. *Physical Review B, 57*(3), 1505–1509.
15. Brillouin, L. (1930). Les électrons libres dans les métaux et le role des réflexions de Bragg. *Journal de Physique et le Radium, 1*(11), 377–400.
16. Monkhorst, H., & Pack, J. (1976). Special points for Brillouin-zone integrations. *Physical Review B, 13*(12), 5188–5192.
17. R. F. Bader, R. F. (1990). *Atoms in Molecules: A Quantum Theory*. Oxford University Press, Oxford.
18. Henkelman, G., Arnaldsson, A., & Jónsson, H. (2006). A fast and robust algorithm for Bader decomposition of charge density. *Computational Materials Science, 36*(3), 354–360.
19. Yu, M., & Trinkle, D. (2011). Accurate and efficient algorithm for Bader charge integration. *The Journal of Chemical Physics, 134*(6), 064111.
20. Villars Pierre and Cenzual, K. (Ed.). (n.d.). Co_3O_4 Crystal Structure: Datasheet from "PAULING FILE Multinaries Edition – 2012"' in SpringerMaterials Available at https://materials.springer.com/isp/crystallographic/docs/sd_0311005
21. Springer-Verlag Berlin Heidelberg & Material Phases Data System (MPDS). Switzerland & National Institute for Materials Science (NIMS), Japan.

N-LEĢĒTĀ Co_3O_4 MODELĒŠANA PĒC PIRMAJIEM PRINCIPIEM

G. Kaptagaja, J. Mastrikovs, J. Kotomins

K o p s a v i l k u m s

N-leģētais Co_3O_4 ir perspektīvs elektrokatalizators. Izmantojot pirmā principa aprēķinus, tika modelētas dažādas N_O atomu koncentrācijas un telpiskās struktūras. Piemaisījuma atomu savstarpējā mijiedarbība tika analizēta attiecībā uz mono N_O atomu. Aprēķināts piemaisījumu radītais lādiņa pārdalījums.

30.08.2018.

sciendo

LATVIAN JOURNAL OF PHYSICS
AND TECHNICAL SCIENCES
2018, N 5

DOI: 10.2478/lpts-2018-0035

MECHANICAL ENGINEERING

NUMERICAL STUDY OF FLOW-INDUCED VIBRATIONS OF MULTIPLE FLEXIBLY-MOUNTED CYLINDERS IN TRIANGULAR ARRAY

S. Upnere

Riga Technical University and Ventspils University College,
36 Viskaļu Str., Riga, LV –1014, LATVIA
*Corresponding author: upnere@gmail.com

The paper presents the numerical study of vibrating multiple flexibly-mounted cylinders in a triangular rod bundle. Behavioural trends of six different clusters of oscillating rods have been analysed. The influence of neighbour cylinders on the central cylinder oscillation characteristics is analysed. Finite volume solver of open source computational fluid dynamics is used to calculate the fluid flow in the channel with the cylinder array. Built-in six degree-of-freedoms solver is utilised to simulate cylinder movement. Oscillating cylinders have two degrees-of-freedom. The obtained results are compared with numerical results available in the literature.

Keywords: *cylinder bundle, computational fluid dynamics, flow-induced vibrations, turbulence*

1. INTRODUCTION

Unscheduled plant shutdowns can cause significant financial losses in the industry or environmental pollution in some specific cases. Therefore, it is important to assess potential problem areas already at the system development stage. The investigation of failure mechanisms has been intensively done to get a better understanding of potentially dangerous processes. Rods or tubes in cross-flow heat exchangers and steam generators or fuel rods of nuclear power plants are subjected to flow-induced vibrations if the oscillation amplitude of the rod exceeds a critical value, failures can occur. These failures include fretting wear between the tubes and the tube supports and fatigue due to cyclical stresses [1]. The possible flow-induced vibration mechanisms are described in [2].

There are many publications about physical and numerical experiments of different aspects of flow-induced vibrations in the case with a single flexible rod or tube

surrounded by the rigid array, for example, [3]–[6]. Analytical and semiexperimental models are also evolved for this simplest case (for more information see a review of Price [7]).

Multiple flexibly-mounted cylinders in the rod array have been studied less. Experimental investigation of a group of three flexibly mounted tubes in an otherwise fixed array has been done by Andjelić et al. [8]. For this case, experimental results prove the existence of three stability boundaries. The instability phenomenon in a tube bundle where the tube flexibility direction is different from the flow direction is investigated in [9]. The authors found that increasing the flexibility angle results in a decrease in the critical velocity of fluidelastic instability (FEI) (description of FEI see in [11]).

Hassan et al. [10] used a Reynolds-averaged Navier-Stokes (RANS) computational fluid dynamics (CFD) solution utilising an arbitrary Lagrangian-Eulerian formulation with moving boundaries to predict fluid force coefficients and combining the coefficient data with unsteady flow model. They got a very good estimation of the FEI of the in-line square and normal triangle array. Jafari and Dehkordi [12] have numerically obtained the FEI onset for seven types of flexible tube bundles in normal triangular arrangements.

This paper presents a numerical study of the closed-packed rod bundle with pitch-to-diameter ratio $P/d = 1.1$, where P is the shortest distance between the cylinders centres and d is the cylinder diameter. The aim of the study is to explore the tendencies of behaviour of flexibly-mounted rods affected by the surrounding rods. CFD-based methods have been used to investigate the groups of multiple flexibly-mounted cylinders surrounded by rigid rods. Calculations are done using solvers of open source CFD toolkit OpenFOAM. The obtained results are compared with findings [12]. Groups of vibrating cylinders consist of three to seven items.

2. METHODOLOGY

The instability has been numerically predicted by the simulation of the unsteady, incompressible and turbulent water cross-flow through the triangular rod array. The two-dimensional modelling has been done to reduce computational costs. The high-performance computational cluster is used for simulations. Rods are described as circular cylinders with diameter d = 0.008 m. Physical and mechanical parameters and simulation conditions used in calculations are summarised in Table 1.

Table 1

Simulation Parameters

	Nomenclature	Value
Fluid density		1000 kg/m^3
Fluid kinematic viscosity		1e-6 m^2/s
Fluid free-stream velocity		0.709 m/s
Mass of cylinders		0.0368 kg
Density of cylinders		7800 kg/m^3
Diameter of cylinders		0.008 m
Pitch-to-diameter ratio		1.1
Turbulence intensity		5%

With subscripts, f and s denote variables related to the fluid and the solid domain, respectively.

2.1. Mathematical Models

The water flow field in the flow domain, $\mathcal{F}(t)$, is governed by RANS equations for steady-state cases and unsteady RANS (URANS) equations (1)–(2) for timedependent cases.

$$\frac{\partial \overline{\boldsymbol{U}}_j}{\partial x_j} = 0 \; in \; \mathcal{F}(t) \; for \; t > 0, \tag{1}$$

$$\left[\frac{\partial \overline{\boldsymbol{U}}_i}{\partial t} + \overline{\boldsymbol{U}}_j \frac{\partial \overline{\boldsymbol{U}}_i}{\partial x_j}\right] = -\frac{1}{\rho}\frac{\partial \bar{P}}{\partial x_i} + \upsilon \frac{\partial^2 \overline{\boldsymbol{U}}_i}{\partial x_j \partial x_j} - \frac{\partial}{\partial x_j}\left\{\overline{\boldsymbol{U}_i \boldsymbol{U}_j}\right\} in \; \mathcal{F}(t) \; for \; t > 0, \tag{2}$$

where bar denotes averaged values, $\bar{\boldsymbol{U}}$ is average velocity, $\bar{P}$ is average pressure, ν is viscosity, ν is time. The problem must be supplemented with the initial condition (3) and Dirichlet boundary conditions (4) for velocity, and Neumann boundary conditions (5) for normal stresses.

$$\boldsymbol{u} = \boldsymbol{u}_0 \; in \; \mathcal{F}(t) \; for \; t = 0, \tag{3}$$

$$\boldsymbol{u} = \boldsymbol{g}_f \; on \; \Gamma_{D,f} \; for \; t > 0, \tag{4}$$

$$\sigma_f \cdot \boldsymbol{n}_f = \boldsymbol{d}_f \; on \; \Gamma_{N,f} \; for \; t > 0, \tag{5}$$

where σ_f is a stress tensor and $\boldsymbol{n}_f$ is a normal vector, $\boldsymbol{u}_0$ is initial velocity in the domain, $\boldsymbol{g}_f$ and $\boldsymbol{d}_f$ are corresponding values on the boundary.

Moving cylinders are described with Eqs. (6)–(7), which are valid for small displacements $\boldsymbol{\eta}$. Boundary conditions have been defined in the solid domain, $\mathcal{S}(t)$, with Eqs. (8)–(9).

$$\rho_s \frac{\partial^2 \boldsymbol{\eta}}{\partial t^2} - \nabla \cdot \sigma_s = \boldsymbol{F}_s \; in \; \mathcal{S}(t), \tag{6}$$

$$\sigma_s = \lambda(\nabla \cdot \boldsymbol{\eta})\boldsymbol{I} + 2\mu\varepsilon, \tag{7}$$

$$\boldsymbol{\eta} = \boldsymbol{g}_s \; on \; \Gamma_{D,s} \; for \; t > 0, \tag{8}$$

$$\sigma_s \cdot \boldsymbol{n}_s = \boldsymbol{d}_s \; on \; \Gamma_{N,s} \; for \; t > 0, \tag{9}$$

where μ and λ are Lamé constants, $\boldsymbol{I}$ is a second rank unit tensor, ε is strain tensor, $\boldsymbol{g}_s$ and $\boldsymbol{d}_s$ are values on the boundary.

On the interface, $\mathcal{I}(t)$, between fluid- and solid-domain kinematic Eq. (10), dynamic Eq. (11) and geometric Eq. (12) coupling conditions have been applied:

$$\boldsymbol{u}_f = \frac{\partial \boldsymbol{\eta}}{\partial t} \; on \; \mathcal{I}(t), \tag{10}$$

$$\sigma_f \cdot \boldsymbol{n}_f = -\sigma_s \cdot \boldsymbol{n}_s \; on \; \mathcal{I}(t), \tag{11}$$

$$\Omega(t) = \mathcal{F}(t) \cup \mathcal{S}(t) \cup \mathcal{I}(t), \; \mathcal{F}(t) \cap \mathcal{S}(t) = 0 \tag{12}$$

The set of Eq. (1), Eq. (2), Eq. (6) and Eqs. (10)–(12) formulates a coupled fluidstructure problem.

2.2. Numerical Implementation

Open source CFD toolkit OpenFOAM 2.4.x has been used to solve 2D differential equations of continuity and momentum (see Eqs. (1)–(2)). Reynolds number based on cylinder diameter and freestream velocity U_∞ is $5.67 \cdot 10^3$. Therefore turbulence should be considered. The following twoequation turbulence models are investigated: standard kepsilon, RNG kepsilon, and realisable kepsilon model, to get the equation system closure.

The numerical procedure is based on a SIMPLE algorithm for steadystate calculations. For coupling the pressure and momentum quantities in transient cases, PIMPLE algorithm [13] is applied. Bounded Gauss linear upwind scheme, which fuses the upwind and linear schemes and is second order, is utilised for calculations. First order implicit, bounded Euler scheme is used for time derivatives.

The equation of motion of the flexibly-mounted cylinder can be written as:

$$(m_s + m_a)\ddot{x}_i + c\dot{x}_i + kx_i = \boldsymbol{F}_f, \tag{13}$$

where m_s is mass of oscillating cylinder, m_a is fluid added mass, c is the damping coefficient, k is the stiffness coefficient and $\boldsymbol{F}_f$ is the fluid force on the oscillating object. Dot denotes the time derivative of the coordinate x_i, $i=1,2$. A fluid dynamic force applied to move the cylinder consists of the damping force due to the fluid, the stiffness force due to the rod displacement and the inertia force due to added fluid mass [14].

Built-in six degree-of-freedom (DoF) OpenFOAM solver is applied. DoF of the oscillating cylinder is reduced to 2 DoF; rotations and transition in the z-direction are not allowed. Mesh modifications are performed after each calculation step. Constant Laplace's equation for the motion displacement has been solved to update the position of points:

$$\nabla \cdot (\gamma \nabla D_m) = 0, \tag{14}$$

where γ is a diffusion coefficient. Distance-based diffusivity model is applied. Solver allows defining the ring-shaped area where a mesh cell cannot be shrunk or expanded due to cylinder oscillations. Therefore, the boundary layer cells of the vibrating cylinder are without undergoing deformations.

The stiffness coefficient of the flexibly-mounted neighbour cylinders is larger than the central cylinder to avoid neighbour cylinders collisions. The damping coefficient is set to zero to get maximum amplitude.

3. COMPUTATIONAL DOMAIN AND ANALYSED CONFIGURATIONS

3.1. Computational Domain

The array contains seven rows of circular cylinders. Based on Weaver and ElKashlan's [15] experimental results of flow-induced vibrations in the tube bundle, it is recommended that six tube rows be used. In the model, each row has three whole cylinders or two whole and two half-cylinders, which provide uniform water flow through the array. Cylinder array consisting of the computational domain and its related parameters are shown in Fig. 1. Grey shaded cylinders labelled "c0" to "c6" can vibrate parallel and perpendicular to the flow direction due to hydrodynamic forces. In the figures below, rigidly fixed rods are filled in white. Two springs have been applied to each oscillating cylinder, one in the vertical and one in the horizontal direction concerning the flow direction. The central moving cylinder is in the fourth row.

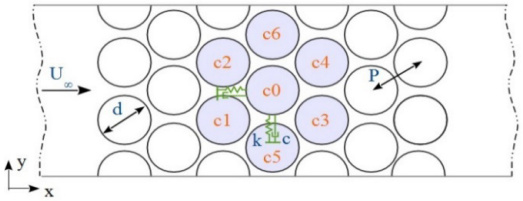

Fig. 1. Cylinders array's part of the computational domain with freestream flow U_∞ direction, cylinder pitch P, cylinder diameter d, stiffness coefficient k and damping coefficient c.

Depending on the case, five combinations of flexibly-mounted cylinder clusters are investigated in the present study. Groups of three, five and seven oscillating cylinders are analysed; all cases are presented in Fig. 2.

The total computational domain is 0.416 m long: 14 d before and 37 d after central cylinder "c0". Building the computational mesh, each cylinder perimeter is divided into 600 parts. The cell size in the radial direction is increased with a growth factor of 1.01 till the 20th cell.

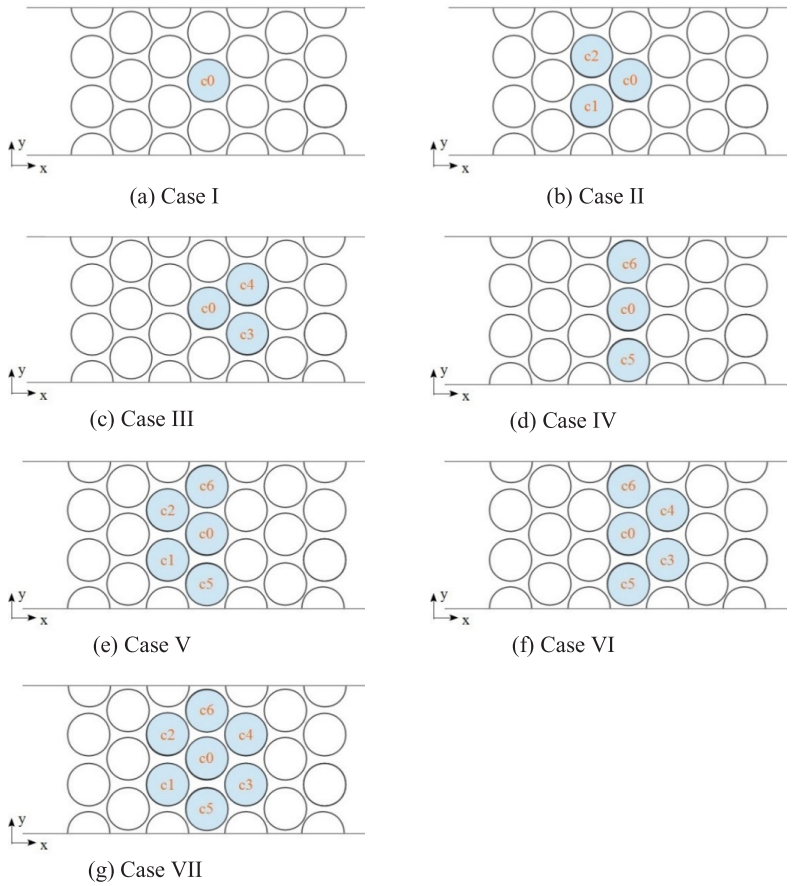

Fig. 2. Analysed groups of the oscillating cylinder (grey shaded).

3.2 Boundary Conditions

Boundary names in the computational domain are shown in Fig. 3.

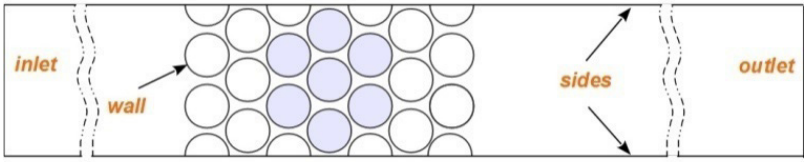

Fig. 3. Boundary conditions of the computational domain.

Constant inlet velocity U, the turbulence kinetic energy k_t and the rate of dissipation of turbulence energy ε_t are defined at the inlet. Pressure is constant at the outlet. On the rigid cylinder walls, the velocity is set to zero. On the channel sides, the symmetry conditions are applied. The used boundary conditions are summarised in Table 2.

Table 2

Boundary Conditions

Name	Type	
	Dirichlet (fixed value)	von Neumann (zero gradient)
Inlet	U, k_t, ε_t	p
Outlet	p	U, k_t, ε_t
Wall	U	p, k_t, ε_t
Sides	Symmetry conditions	

4. RESULTS AND DISCUSSION

Numerical calculations are initiated with a series of quasi-steady-state simulations in a 2D domain where all cylinders in the array are static. These tests have been used to select calculation parameters such as boundary conditions, the turbulence models and to investigate the effect of cell size on results. Based on the comparison of the numerically predicted pressure drop with experimental results of the water channel in [16], the model validation has been done. The renormalisation group (RNG) k-epsilon turbulence model is chosen. The steady-state cases are assumed to be converged if residuals are less than 10^{-8}. The coefficients for the model are given in Table 3. The quasi-steady simulation results are used as initial conditions for the dynamic modelling.

Table 3

RNG k-Epsilon Turbulence Model Coefficients

β	η_0	σ_k	σ_k	C_μ	C_1	C_2
0.012	4.38	0.7194	0.7194	0.0845	1.42	1.68

In transient cases, the time step is chosen to correspond to approximately 140 steps per cycle. The suggested resolution of the time step by [10] and [17] is from 35–100 steps per oscillation period; therefore, it can be considered small enough not to affect the simulation results.

The time-dependent simulations have been started with single flexibly-mounted cylinder “c0” in the rigid rod bundle (see in Fig. 2(a)). The major movement of “c0” corresponds to the direction of the freestream flow (see Fig. 4(a)); it fits with experimental measurements of [16], but it disagrees with [12] where cylinders vibrate more in a direction perpendicular to the flow. As follows from Fig. 4, additional flexibly-mounted neighbour cylinders increase the vibration amplitude of the central cylinder “c0”.

Three groups of three flexible cylinders (Case II, Case III and Case IV) and two groups of five oscillating cylinders (Case V, Case VI) in the rigid array are simulated. The influence of free to vibrate neighbour cylinders in transverse direction on the central cylinder oscillation amplitude is smaller comparing to upstream and downstream cylinders (see Cases II–IV). Due to the flow symmetry, the dynamic response of cylinders in pairs “c1”–“c2”, “c3”–“c4” and “c5”–“c6” is similar but in

opposite direction, it coincides with findings in [12]. The vibration is dominant in the lift direction of cylinders “c5” and “c6”, except for Case IV.

The seven-cylinder cluster configuration (Case VII) can be considered the unit that has been proposed to model a fully flexible rod bundle. As in all preview cases, flexible cylinder trajectory orbits are elliptic. The wake effect of “c3” and “c4” is strongly expressed if we compare Case VI and Case VII with Case III.

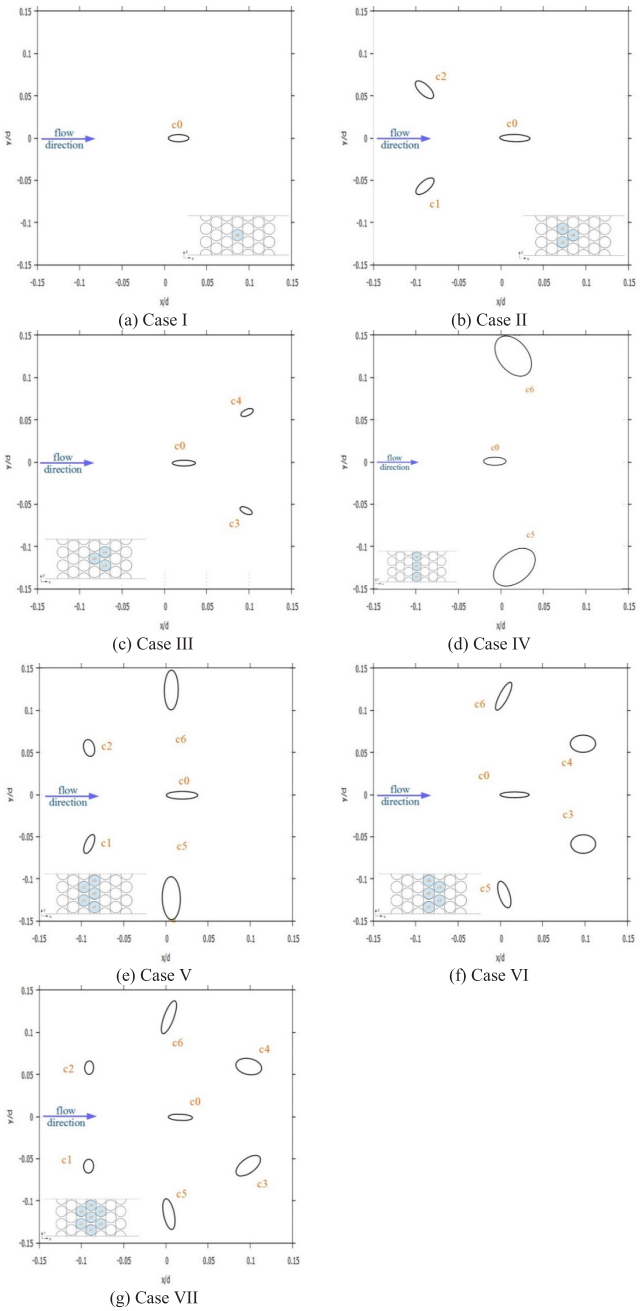

Fig. 4. The vibration orbits of flexibly-mounted cylinders. Displacements in x and y-direction are divided by cylinder diameter.

The oscillation frequencies, f_{oscil} of the central cylinder "c0" for all cases are summarised in Table 4. The frequency of "c0" is similar in Case I and Case VI, where upstream and downstream cylinders are not flexibly-mounted. The frequency of "c0" increases if the movement of cylinders "c1" to "c4" is allowed.

Table 4

The Oscillation Frequencies of Central Cylinder

	Cases					
	Case I	Case II	Case III	Case VI	Case V	Case VII
f_{oscil}	69.63 Hz	83.87 Hz	80.25 Hz	68.72 Hz	91.63 Hz	80.25 Hz

Simulation results show that in cases when upstream cylinders are flexible (Case II and Case V), the oscillation frequency of central cylinder increases if compared with cases where downstream cylinders vibrate.

5. CONCLUSIONS

The flow-induced vibrations have been predicted using numerical simulations of water flow through groups of flexibly-mounted cylinders in otherwise rigid rod array of the triangular arrangement. To model turbulence, the RNG k-epsilon turbulence model has been used. For validation of CFD results, the simulations of the rigid cylinder array and calculated pressure drop comparison with experimental results have been made. The quasi-static results have been applied as initial conditions for transient simulations.

The single flexibly-mounted cylinder in the rigid array, as well as six groups with three, five or seven flexible cylinders have been studied to find the major tendencies in the closed-packed tube bundle related to the flow-induced vibrations.

The interaction between the fluid and the solid rods in a triangular rod bundle has been modelled using a six degree-of-freedoms solver. In the case when upstream or downstream cylinders are flexibly mounted, the central cylinder becomes more unstable.

There are no significant differences in the oscillation frequency of central cylinder observed comparing the case of the single flexibly-mounted cylinder with the case where upper and lower cylinders are flexible.

REFERENCES

1. Vincent, B.T., Hassan, M.A., & Rogers, R.J. (2009). A probabilistic assessment technique applied to a cracked heat exchanger tube subjected to flow-induced vibration. *Journal of Pressure Vessel Technology*, *131*, 031305-1-6. DOI: 10.1115/1.3109989
2. Weaver, D.S., & Fitzpatrick, J.A. (1988). A review of cross-flow induced vibrations in heat exchanger tube arrays. *Journal of Fluids and Structures*, *2*, 73–93. DOI: 10.1016/S0889-9746(88)90137-5
3. Khalifa, A., Weaver, D., & Ziada, S. (2012). A single flexible tube in a rigid array as a model for fluidelastic instability in tube bundles. *Journal of Fluids and Structures*, *34*, 14–32. DOI: 10.1016/j.jfluidstructs.2012.06.007

4. de Pedro, B., Parrondo, J., Meskell, C., & Oro, J. F. (2016). CFD modelling of the cross-flow through normal triangular tube arrays with one tube undergoing forced vibrations or fluidelastic instability. *Journal of Fluids and Structures*, *64*, 67–86. DOI: 10.1016/j.jfluidstructs.2016.04.006
5. Charreton, C., Béguin, C., Yu, K.R., & Étienne, S. (2015). Effect of Reynolds number on the stability of a single flexible tube predicted by the quasi-steady model in tube bundles. *Journal of Fluids and Structures*, *56*, 107–123. DOI: 10.1016/j.jfluidstructs.2015.05.004
6. Mahon, J., & Meskell. C. (2013). Estimation of the time delay associated with damping controlled fluidelastic instability in a normal triangular tube array. *Journal of Pressure Vessel Technology*, *135*, 030903-1-7. DOI: 10.1115/1.4024144
7. Price, S.J. (1995). A review of theoretical models for fluidelastic instability of cylinder arrays in cross-flow. *Journal of Fluids and Structures*, *9*, 463–518. DOI: 10.1006/jfls.1995.1028
8. Andjelić, M., Austermann, R., & Popp, K. (1992). Multiple stability boundaries of tubes in a normal triangular cylinder array. *Journal of Pressure Vessel Technology*, *114*, 336–343. DOI: 10.1115/1.2929049
9. Khalvatti, A., Mureithi, N.W., & Pettigrew, M.J. (2010). Effect of preferential flexibility direction on fluidelastic instability of a rotated triangular tube bundle. *Journal of Pressure Vessel Technology*, *132*, 041309-1-14. DOI: 10.1115/1.4002181
10. Hassan, M., Gerber, A., & Omar, H. (2010). Numerical estimation of fluidelastic instability in tube arrays. *Journal of Pressure Vessel Technology*, *132*, 041307-1-11. DOI: 10.1115/1.4002112
11. Ibrahim, R.A. (2011). Mechanics of pipes conveying fluids - Part II: Applications and fluidelastic problems. *Journal of Pressure Vessel Technology*, *133*, 024001-1-30. DOI: 10.1115/1.4001270
12. Jafari, H.H., & Dehkordi, B.G. (2013). Numerical prediction of fluid-elastic instability in normal triangular tube bundles with multiple flexible circular cylinders. *Journal of Pressure Vessel Technology*, *135*, 031102-1-14. DOI: 10.1115/1.4023298
13. Holzmann, T. (2017). Mathematics, numerics, derivations and OpenFOAM (4th ed.). Leoben: Holzmann CFD.
14. Kim, S.N., & Jung, S.Y. (2000). Critical velocity of fluidelastic vibration in a nuclear fuel bundle. *Korean Society of Mechanical Engineers International Journal, 14*(8), 816–822.
15. Weaver, D.S., & El-Kashlan, M. (1981). On the number of tube rows required to study cross-flow induced vibrations in tube banks. *Journal of Sound and Vibration*, *75*(2), 265–273. DOI: 10.1016/0022-460X(81)90344-8.
16. Upnere, S., Jekabsons, N., & Dementjevs, S. (2016). Analysis of cross-flow induced vibrations in staggered arrangement of multi-cylinder system. In *5th European Seminar on Computing*, 5–10 June 2016 (pp. 225). Pilsen, Czech Republic.
17. Lam, K., Jiang, G.D., Liu, Y., & So, R.M.C. (2006). Simulation of cross-flow-induced vibration of cylinder arrays by surface vorticity method. *Journal of Fluids and Structures*, 22, 1113–1131. DOI: 10.1016/j.jfluidstructs.2006.03.004

SKAITLISKS PĒTĪJUMS PAR PLŪSMAS IZRAISĪTĀM VIBRĀCIJĀM TRĪSSTŪRVEIDA MASĪVĀ AR VAIRĀKIEM ELASTĪGI NOSTIPRINĀTIEM CILINDRIEM

S. Upnere

K o p s a v i l k u m s

Stieņi un caurules siltummaiņos, tvaika ģeneratoros vai kodolspēkstaciju degvielas stieņos tiek pakļauti plūsmas izraisītām vibrācijām. Ja stieņa svārstību amplitūda pārsniedz kritisko vērtību, tad var rasties bojājumi sistēmā. Neplānota iekārtu slēgšana atsevišķos gadījumos var radīt ievērojamus finansiālus zaudējumus vai vides piesārņojumu, tādēļ ir svarīgi novērtēt potenciālās problēmas jau sistēmas izstrādes posmā.

Aprakstītais darbs ir saistīts ar vairāku elastīgi nostiprinātu stieņu uzvedību plūsmas ietekmē daudzstieņu sistēmā. Tiek analizētas sešu dažādu oscilējošo stieņu grupu uzvedības tendences šķērsplūsmā. Tiek novērtēta blakus esošo cilindru ietekme uz centrālā cilindra svārstību īpašībām. Atvērtā koda skaitliskās hidrodinamikas programmatūra tiek izmantota, lai aprēķinātu šķidruma plūsmu kanālā, kas satur masīvu ar septiņām cilindru rindām. Iegūtie rezultāti tiek salīdzināti ar literatūrā pieejamiem skaitliskiem rezultātiem.

24.07.2018.

sciendo

LATVIAN JOURNAL OF PHYSICS
AND TECHNICAL SCIENCES
2018, N 5

DOI: 10.2478/lpts-2018-0036

APPLIED PHYSICS

THE INFLUENCE OF ICE TEXTURE ON SLIDING OVER ICE

E. Jansons[1,2*], K.A. Gross[1], J. Lungevics[1,2], L. Pluduma[1]

[1]Biomaterials Research Laboratory
Riga Technical University
3 Paula Valdena Str., Riga, LV-1048, LATVIA
[2]Institute of Mechanical Engineering
Riga Technical University
36a Viskalu Str., Riga, LV-1006, LATVIA
[*]e-mail: Ernests.Jansons_1@rtu.lv; kgross@rtu.lv

Winter brings snow and ice to Northern Europe and with it the need to move safely over ice. It has been customary to select an appropriate material surface for movement over ice, but another way to influence the interaction with ice is to appropriately prepare the ice surface. The objective of the research is to investigate the influence of ice texture on initiating movement over ice and on sliding velocity over ice in the laboratory and field conditions. The ice has been prepared smooth, scratched and glazed similar to the one found in real life situations. The static coefficient of friction and the sliding speed have been measured at the laboratory, but the sliding speed quantified on a skeleton – at the skeleton push-start facility. The scratched ice surface has increased the resistance to movement, thus resulting in the lowest sliding speed under laboratory conditions. Sliding is better on the smooth ice and glazed ice. The contact surfaces have been measured to determine the effect of contact area on sliding properties. Field experiments with heavier loads have flattened the ice surface irregularities for more constant sliding conditions over time. This outcome provides a useful indicator for pedestrians and road traffic related to the safety of movement over different ice surfaces as well as a reference for those involved in winter sports.

Keywords: *contact area, ice friction, inclined plane, ice texture, sliding velocity, tribology*

1. INTRODUCTION

Ice surface in real life situations forms in different ways because freezing is strongly affected by weather conditions and other external influences from society. In nature, different ice surfaces can be observed around us. For example, if the precipitation under changing weather conditions turns from snow to rain, it is likely that raindrops freeze and form spherical droplets on the surface, thus making a wavy texture. Another situation can be observed if the air temperature drops after wet weather conditions and the ice surface of the puddle or other standing water is smooth. In the field of winter sports, the ice surface can be even more important to achieve the best results especially if athletes use the track one after another; the ice conditions between the first and the last participant could be significantly different. Despite the active research on the interaction between ice and the sliding object, there is little or no mention of the ice texture. The knowledge of how ice texture affects the sliding speed can be valuable in the sports industry, transportation sector and provide new insights for those involved in research. This study will emphasise the importance of ice texture in ice tribology.

The interaction between ice and solid object is one of the most complicated tribological systems due to many influencing factors such as contact pressure, surface roughness, hydrophobicity, macro geometry of the object, ice and ambient temperature, relative humidity, liquid like layer (LLL) thickness, etc. Nevertheless, usually ice surface texture is not characterised enough believing that effect on the results is not significant. The lack of an easy-to-use methodology for characterisation of the ice surface is another reason for poorly described texture of ice in many previous studies.

The ice contact area can be determined by making a replica of the ice surface. Using this method, Baurle et al. [1] measured 2D ice roughness and observed a 4-fold difference in the average roughness Pa (arithmetical mean height for primary profile) between undisturbed ice (0.07μm) and ice on the ice track (0.3μm). A similar approach with ice replicas by Spagni et al. [2] reported an average roughness parameter Ra (arithmetical mean height for roughness profile) of 0.1μm ±0.01.

Two dimension roughness measurements provide an insight, but a 3D measurement is required for more detail. Ducret et al. [3] previously used textured moulds to produce different ice surface textures in order to measure the effect of ice roughness on the coefficient of friction (COF). The surface texture of moulds was measured in 3D (across the entire surface). Using an angle between a sliding object and ice asperities surface smoothness was determined. The COF measurements from two different ice surfaces showed a 4-fold increase in COF by changing ice texture from a smooth surface to a more glazed ice.

Contact area between ice and sliding object is one of the main factors influencing the movement over ice. Measuring sliding friction of polyethylene over ice, Baurle et al. [1], [4] concluded that the main factors influencing friction over ice were a real contact area and a liquid-like layer. It was observed that the coefficient of friction increases as a contact area increases. Rohm et al. [5] investigated the influence of metal ski surface roughness on the coefficient of friction. It was concluded that smoother surfaces with a larger contact area had a higher COF than rough surfaces. As a result, adhesion force increased which resulted in higher COF between

metal ski and suppressed snow. A higher COF was observed at warmer temperatures, when the liquid-like layer was thicker and the adhesion force was higher. The effect of the contact area was lower at lower temperatures and faster velocities. Using calculations, Scherge et al. [6] stated that a higher contact area could lead to increased velocity due to a thicker film of the melt water.

To investigate the significance of the ice surface texture on the tribological properties between ice and the moving object, three fundamentally different ice surfaces have been created to determine the static coefficient of friction and sliding speed. In order to perform such experiments, two devices based on the inclined plane principle have been used at the laboratory. Both of these devices have previously been tested and proven to be reliable and useful for such tests [7]. Results are analysed taking into account the contact area between ice and sliding object; the contact area has been measured with a simple test method that shows the top surface. The goal of the study is to demonstrate how object sliding speed and the coefficient of friction are affected by different ice textures.

2. MATERIALS AND METHODS

2.1. Experimental Setup

Laboratory Setup

Laboratory experiments have been conducted under controlled ambient conditions in a cold room (W/L = 3.5 m, H = 2.2 m). Two inclined plane principle based devices have been used to study tribological properties between ice and stainless steel:

a. Sliding speed of the laboratory samples has been measured on a 3.3 m long ice track. The track angle has been set to 16 ° and remained constant throughout all experiments. This plane angle has been chosen to ensure sliding a stationary position, and provide a long enough sliding time to detect differences on various ice textures. Sliding speed has been measured using four retroreflective sensors arranged along the length of the track [7].
b. The static coefficient of friction has been measured using a shorter inclined plane as shown in Fig. 1. The angle α of the initially horizontal ice track is slowly increased until the sample overcomes static friction and initiates sliding down the plane. To initiate sliding, the plane angle is noted at an accuracy of 30`. The static coefficient of friction (COF) has been calculated as tangent of the measured angle.

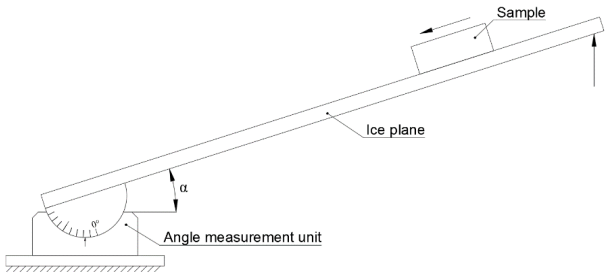

Fig. 1. Principal scheme of the static coefficient of friction.

Experimental samples have been made from an International Bobsleigh and Skeleton Federation (IBSF) standardised austenite structure stainless steel (62 % Fe; 15.8 % Ni; 13.8 % Cr; 5 % Mo; 1.4 % Co; 1.2 % Mn; 0.8 % Cu) as rectangular blocks with dimensions of 35 x 18 x 14 ±0.2 mm and weight of 67 ± 0.5 g. The material has been chosen because of its good anti-corrosion properties.

Samples have been milled from one workpiece and the sliding surface made smooth by grinding and polishing on an automated polisher – Mecatech 334 TI 15 (Presi, FRA) to an average surface roughness, Sa, ~ 10 nm. Before experiments, samples have been placed in the cold room to cool down for at least 10 minutes. Gloves with low thermal conductivity have been used while working with samples to prevent sample heating.

Field Experiment

A 24-m long ice-track located in Sigulda bobsleigh track push-start training facility has been used for field tests. The experiment setup has not provided full control of the ambient conditions, but the ice surface has still been protected from the influence of wind, snow and sun [8].

The track has been equipped with two optical sensor pairs (four sensors in total), which has allowed measuring the sliding speed of the skeleton sled while its moving down an angled plane. The ice track has been protected from wind, snow and sun, but a grill on the floor enabled air circulation for the temperature and relative humidity to equilibrate with the outside conditions. A U-shaped groove (20 mm diameter) has been formed in the ice track in order to guide the skeleton along the same path for every run.

The skeleton sled has been used as an experimental sample due to its relatively simple construction and relatively large runner contact area with ice. Runners that were 1000 mm long and 16 mm wide freely sat in the U-shaped ice groove. The runners are made of the same austenite structure steel as laboratory samples and polished manually using 3000 grade sand paper, to a surface roughness Sa of ~ 0.14 μm. Metallic debris and sandpaper particles after polishing have been removed with a tissue soaked in ethanol. After cleaning, the sled has been placed on the ice surface for at least 10 minutes to even runner and ice temperature.

2.2. Preparation of Ice and Contact Area Measurements

On laboratory track, boiled tap water (~70° C) has been poured into the horizontally levelled U-shaped channel, layer by layer, to ensure homogenous ice without cracks and air inclusions. Every next layer has been added after previous one has been frozen. A total of 5 layers have been collected to fill the entire channel volume. When the ice has been frozen, a small groove has been placed in the ice surface with a planer. The groove has ensured that the steel blocks have followed the same path. The planer has also made a flat base before making changes to the ice texture.

Similarly as in laboratory, the base of the 24-m long ice track has been formed

layer by layer using hot water to fill pores and cracks in the previous layer only this time the number of layers is significantly larger. Once the desired thickness is achieved, the ice surface is planned and a straight groove with a diameter of 20 mm is made in the ice in order to guide one runner of the skeleton.

Ice has been made to three different ice textures – smooth, scratched and glazed. To prepare a smooth surface (Fig. 2.a), a thin layer of boiled water (~70° C) has been poured into previously planned inclined plane groove and then frozen for 10 to 20 minutes, based on the chosen air temperature. In order to prepare scratched surfaces (Fig. 2.b), a 60 grade sandpaper (Klingspor) has been used to prepare scratches parallel and perpendicular to the motion of the sliding body. After ice is scratched, particles from sandpaper and ice debris are carefully removed using a brush. For surface with solidified ice droplets (glazed ice), an atomiser has been used to simulate small rain droplets (Fig. 2.c). Cold water (~2° C) has been sprayed ~20 cm from the ice surface. Water temperature has been kept at 2°C in order to minimise the temperature difference between the droplet and the ice surface.

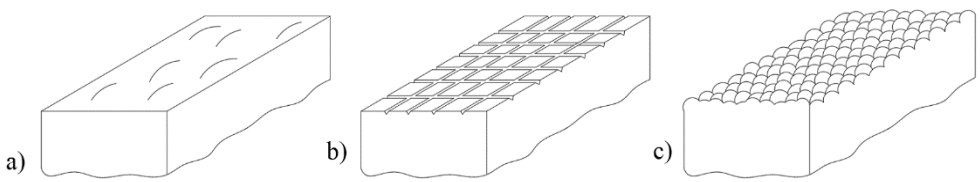

Fig. 2. Ice surfaces: a) Smooth; b) Scratched; c) Glazed.

All ice textures have been imaged using a 1000 x USB Digital Microscope (Gaosuo, CHN) from both the laboratory and the push-start facility. This type of microscope has been chosen because it can be easily transported and could be used in cold conditions.

In order to estimate the ice contact area, a method has been used to highlight the top surface. Water-based black ink has been poured on the modified ice surface that drained to the lower areas of all the modified surfaces. Microscope images have been processed with Photoshop (Adobe, USA) software to determine the percentage of "black" and lighter areas of each image. The lighter areas representing the higher points on ice have been presumed to be the contact surface with a sliding object. This simple, fast and practical method for measuring the top surface has provided an alternative to contact surface measurements from ice-replicas and profilometry experiments.

2.3. Experimental Settings

Three different experiments have been conducted to determine sliding of stainless steel on various ice textures: a) sliding speed at the laboratory, b) the static coefficient of friction at the laboratory, c) sliding speed of the skeleton at the push-start facility. Experimental conditions are summarised in Table 1.

Table 1

Experimental Settings

Settings	Laboratory experiments		Field experiments
	Sliding velocity	Static coefficient of friction	Sliding velocity
Air temperature (°); (Relative humidity)	-6.0; (70 %)	-6.0; (70 %)	Day 1: -1.0; (85 %) Day 2: -4.0; (72 %) Day 3: -4.0; (75 %) Day 4: -9.0; (70 %)
Ice temperature, (°)	-5.0	-5.0	Day 1: -4.0 Day 2: -5.0 Day 3: -5.0 Day 4: -9.0
Experimental sample	Rectangular stainless steel block	Rectangular stainless steel block	Skeleton sled with two stainless steel runners
Surface roughness, (μm)	0.01 ± 0.02	0.01 ± 0.02	0.14 ± 0.04
Load	67 ± 0.5 g	67 ± 0.5 g	95 ± 0.2 kg
Experimental days	4	4	4
Experimental samples	4	4	1 sled with 2 runners
Total measurements for one sample	240	120	60

* Variation in the air and ice temperature is ± 1 °C; in air humidity ± 2 %

The temperature and humidity at the laboratory have been set to the same conditions to test for repeatability. The field experiments at the push-start facility provide different conditions for all four experimental days. The air temperature and humidity have been measured with a P330 Temp (Dostmann, GER), and ice surface temperature has been measured with a contact thermocouple TP-122-100-MT-K (Czaki, PL) plugged in Proscan 520 (Dostmann, GER) thermometer for both laboratory and field experiments.

A total of four rectangular stainless steel blocks with the same weight, surface texture and dimensions have been used for laboratory experiments. In field experiments, the surface of the skeleton runners has been manually re-polished before each experimental day. The laboratory and field experiments have shown sliding under different contact pressures.

Total number of tests performed for one sample at the laboratory has been 240 for sliding speed experiments and 120 for coefficient of friction experiments. Field experiments involved a total of 60 sliding speed measurements. A large number of the measurements have provided statistically reliable data.

3. RESULTS AND DISCUSSION

3.1. Ice Surface Contact Area

Images from five randomly chosen locations have been taken for each ice texture (see examples in Fig. 4.) and the average contact area has been calculated.

Contact area ("grey" colour in Fig. 4.) has been determined as a percentage of the total surface area from the images. The estimated contact area has been 97 ± 1 % for smooth ice; 81 ± 1 % for scratched ice and 38 ± 5 % for glazed ice. The random distribution of ice droplets on glazed ice has resulted in an uneven ice texture and a corresponding large variation (5 %).

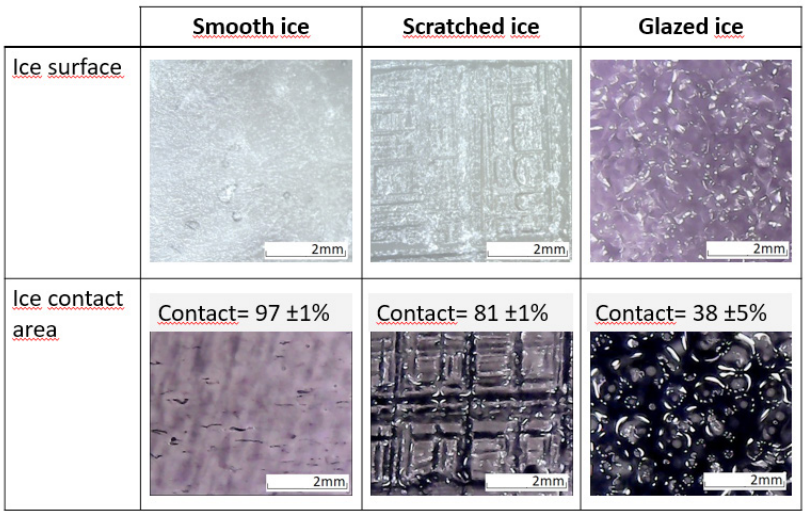

Fig. 4. The ice surface and the contact area of smooth, scratched and glazed ice.

3.2. Laboratory Experiments

Static Coefficient of Friction

Static coefficient of friction (COF) has been calculated as an average of 120 measurements for each ice surface. The smallest COF value (0.072 ± 0.018) has been observed on the glazed ice (Fig 5a). Approximately 1.6 times larger COF values (0.117) have been observed for smooth and scratched ice with standard deviations of 0.033 and 0.022, respectively

The error varies depending on the ice texture. Standard deviation that is almost 2 times higher for smooth ice surface measurements can be explained with a large contact area (97 % for smooth ice surface) between ice surface and experimental sample; this is believed to create an increase in the number of capillary bridges between the sliding surface and ice [9]. Capillary bridges vary in each experiment, contributing to the scatter in the results. Increasing the thickness of the so-called "liquid-like layer" has been suggested to increase the adhesive force between the sliding object and ice resulting in more variable results. A similar explanation can be given to the small static coefficient of friction on glazed ice; the small contact area reduces adhesion between surfaces, but the similar surface area of smooth and scratched ice is not sufficient to differentiate the results. Similar observations about the scatter of the results were found by Baurle et al. [4] with pin-on-disc tribometer tests where an increase in contact area gave a larger variation of the results.

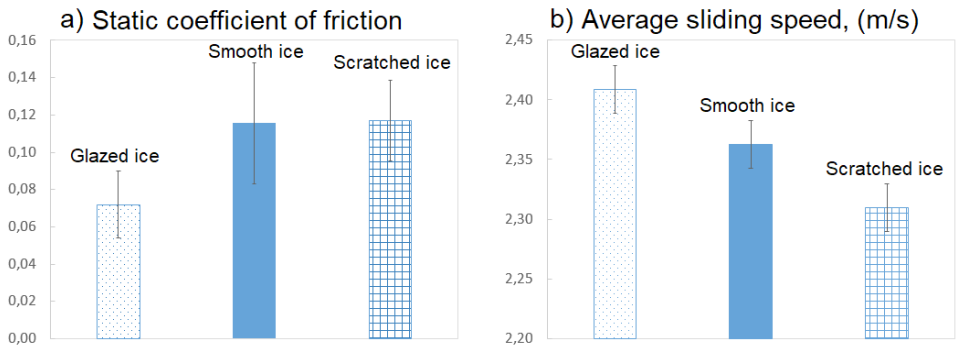

Fig. 5. The co-efficient of friction and the sliding speed for glazed ice, smooth ice and scratched ice show easier sliding on glazed ice.

Sliding Speed

Faster sliding on ice has presented a lower contact with the sliding object. The average sliding speed for the laboratory samples has been calculated from at least 960 measurements on each type of the ice surface (Fig. 5.b.). Similar tendencies for sliding speed appear on all experimental days. The highest sliding speed has been observed on glazed ice (2.409 m/s); on smooth ice, the sliding speed has been reduced by ~ 2 % (2.363 m/s) while the lowest sliding speed (2.310 m/s) has been observed on the scratched ice (~ 4 % slower).

The experiments have clearly demonstrated that faster sliding occurs on glazed ice. The best tribological results for the glazed ice are most likely achieved due to a small contact area (38 %), which reduces overall adhesion forces between surfaces, and the curved form of the ice droplets, which provide easier movement of the sample. Scratched and smooth ice texture provides almost identical static coefficient of friction, but sliding velocity experiments have shown that smooth surface provides better sliding conditions.

Similar tendencies about the influence of the contact area are available in other studies. A metal ski sliding over snow has shown similar results [5]. In Rohm's experiments, the tribological system is opposite to our work, i.e., snow surface is relatively constant while the used skis have different roughness. It was observed that the smallest coefficient of friction resulted from the roughest skies and the tendencies increased with temperature. Rohm et al. considered that such phenomena occured because smoother surfaces had less available volume for the meltwater to spread causing a larger increase in the contact area compared to rougher surfaces. Increase of the contact area increases adhesion and slows movement over ice. Similar findings have been reported from a large-scale rotation tribometer indicating a larger friction from a larger contact surface area [4]. Repeated traverse over the same ice section in rotation tribometer experiments combine the effect of contact area and a thicker water film (that otherwise occurs in warmer conditions) thereby showing a more accentuated effect from the two separate factors, contact area and warmer conditions.

3.3. Field Sliding Experiments

Field tests have been performed using a skeleton as a sliding body to understand the effect of surface contact area under greater contact pressures. The contact pressure from the skeleton has been sufficient to plastically deform the rougher to a smoother surface (Fig. 6).

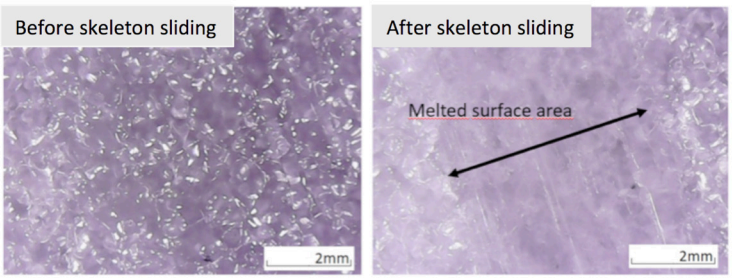

Fig. 6. A glazed ice surface before and after sliding of the skeleton.

Tribological properties of textured ice (glazed and scratched) have changed over time with repeated runs. The sliding speed has changed for the first four runs and then stabilised (Fig. 7).

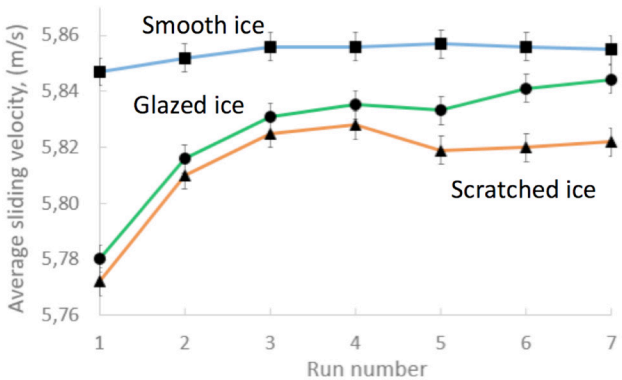

Fig. 7. Sliding velocity ice surfaces. Markers in the graph represent the average sliding velocity of each run calculated from four different experimental days. Dots are used for glazed ice, triangles represent scratched ice and squares represent smooth ice.

The trend of the sliding velocity has remained the same during all experimental days – first run is always the slowest one and sliding velocity increases until it stabilises after ~4 runs. Frozen droplets and scratches on ice surface interfere with the sled runners; as a result, sled runner melts and squeezes the frozen droplets or builds up edges from scratching, thus smoothening the groove. Rohm et al. studied the metal samples against compressed snow, and also showed that measurement values were changing from one measurement to the next, only the observed tendency was opposite, i.e., during first runs smaller COF value was achieved and after approximately 3 runs the measurement results stabilized. It is interesting to note that this phenomenon is more noticeable on smoother surfaces [5].

The observed effect of ice surface modification is opposite for the lighter laboratory samples than for the heavier skeleton in field experiments. If the contact pressure caused by a sliding object is smaller than the yield stress of frozen droplets, improvement of the sliding motion can be observed because the contact area of ice is reduced. But if the pressure of a sliding object is high enough, some of the kinetic energy is dissipated into plastic deformation of the ice surface. Winter sports athletes (skeleton, bobsleigh and luge riders) can therefore expect different results after an increase in the ice contact surface.

The experiments have shown the effect of contact area on sliding speed and emphasised the importance of ice texture. Since the ice contact area is important, further work will evaluate the best method for assessing the contact area, by comparing this method with the use of a replica [4], [2].

Laboratory and field experiments have demonstrated how the contact pressure changes ice tribological properties. Experiments at the laboratory have shown that the glazed ice surface with the smallest static coefficient of friction results in the fastest sliding speed. Further research could address different droplet shapes and the ambient temperature/humidity to study the effect of contact area in more detail.

4. CONCLUSIONS

Ice surface texture has a significant impact on sliding speed over ice in both small-scale and large-scale situations. For lighter sliding objects, a smaller contact area apparently reduces the adhesive force between ice for easier sliding. A larger contact area produces a larger coefficient of friction. Large-scale objects deform surface irregularities, leading to changing sliding conditions until a constant speed is reached.

Quick and direct quantification of the ice contact area measures the ice contact surface without the use of specialised devices or ice replicas.

ACKNOWLEDGEMENTS

The research has been supported by the ERAF project "The Quest for Disclosing how Surface Characteristics Affect Slideability" (No.1.1.1.1/16/A/129). Researchers would also like to acknowledge ice preparation team of Sigulda push-start facility for helping prepare field experiments.

REFERENCES

1. Baurle, L., Kaempfer, T.U., Szabo, D., & Spencer, N.D. (2007). Sliding friction of polyethylene on snow and ice: Contact area and modeling. *Cold Reg. Sci. Technol., 47*, 276–289. doi:10.1016/j.coldregions.2006.10.005
2. Spagni, A., Berardo, A., Marchetto, D., Gualtieri, E., Pugno, N.M., & Valeri, S. (2016). Friction of rough surfaces on ice: Experiments and modeling. *Wear*, 368–369, 258–266. doi:10.1016/j.wear.2016.10.001
3. Ducret, S., Zahouani, H., Midol, A., Lanteri, P., & Mathia, T.G. (2005). Friction and abrasive wear of UHWMPE sliding on ice. *Wear*, 26–31. doi:10.1016/j.wear.2004.09.0264.

4. Baurle, L., Szabó, D., Fauve, M., Rhyner, H., & Spencer, N.D. (2006). Sliding friction of polyethylene on ice: Tribometer measurements. *Tribol. Lett., 24*, 77–84. doi:10.1007/s11249-006-9147-z
5. Rohm, S., Hasler, M., Knoflach, C., van Putten, J., Unterberger, S.H., Schindelwig, K. … Nachbauer, W. (2015). Friction between steel and snow in dependence of the steel roughness. *Tribol. Lett., 59*, 27. doi:10.1007/s11249-015-0554-x
6. Scherge, M., Böttcher, R., Spagni, A., & Marchetto, D. (2018). High-speed measurements of steel–ice friction: Experiment vs. calculation. *Lubricants, 6*, 26. doi:10.3390/lubricants6010026
7. Lungevics, J., Jansons, E., & Gross, K.A. (2018). An ice track equipped with optical sensors for determining the influence of experimental conditions on the sliding velocity. *Latv. J. Phys. Tech. Sci., 55*, 64–75. doi:10.2478/LPTS-2018-0007
8. Jansons, E., Lungevics, J., Stiprais, K., Pluduma, L., & Gross, K.A. (2018). Measurement of sliding velocity on ice, as a function of temperature, runner load and roughness, in a skeleton push-start facility. *Cold Reg. Sci. Technol.*, *151*, 260–266. doi:10.1016/J.COLDREGIONS.2018.03.015
9. Kietzig, A.-M., Hatzikiriakos, S.G., & Englezos, P. (2009). Ice friction: The effects of surface roughness, structure, and hydrophobicity. *J. Appl. Phys.*, *106*, 24303. doi:10.1063/1.3173346

LEDUS TEKSTŪRAS IETEKME UZ SLĪDĒŠANAS PROCESU PA LEDU

E. Jansons, K.A. Gross, J. Lungevičs, L. Plūduma

K o p s a v i l k u m s

Ziemeļu reģionā dzīvojošajiem cilvēkiem jārēķinās ar ziemu, kas rada apledojumu, pa kuru visi vēlas droši pārvietoties. Līdz šim slīdēšana pa ledu pamatā apskatīta no slīdošā objekta topogrāfijas viedokļa, bet šo procesu iespējams ietekmēt arī citādi, t.i., mainot ledus tekstūru. Šīs publikācijas mērķis ir apskatīt kā ledus topogrāfija ietekmē objektu spēju sākt slīdēt uz ledus virsmas, kā arī to, kā ledus virskārta ietekmē parauga slīdēšanas ātrumu gan laboratorijas, gan lauka eksperimentos. Tika sagatavots trīs dažādu tekstūru ledus – gluds, skrāpēts un ar uzsmidzinātām pilītēm, lai imitētu trīs dabā bieži sastopamus ledus tekstūras variantus. Laboratorijas apstākļos ledum veikti miera stāvokļa berzes koeficienta un slīdēšanas ātruma mērījumi, bet lauka eksperimentos skeletona starta treniņa estakādē pārbaudīta ledus tekstūras ietekme slīdēšanas ātrumu. Laboratorijas apstākļos skrāpētā ledus tekstūra uzrādīja sliktāko slīdēšanas ātrumu, kam seko gludais ledus, bet ar pilītēm apsmidzinātais ledus uzrāda labākos slīdēšanas ātrumus. Tika veikti vienkāršoti ledus tekstūras kontakta laukuma mērījumi, lai redzētu atbalsta laukuma ietekmi slīdēšanas uz procesa gaitu. Laboratorijas eksperimentos iegūtie dati tiek pārbaudīti lauka eksperimentos, izmantojot lielāka mēroga virsmas un piespiešanas spēkus. Iegūtie dati var būt noderīgi drošākas kustības pa ledu veicināšanai civilajiem iedzīvotājiem, kā arī ar ziemas sporta veidu pārstāvjiem.

04.09.2018.

sciendo

LATVIAN JOURNAL OF PHYSICS
AND TECHNICAL SCIENCES
2018, N 5

DOI: 10.2478/lpts-2018-0037

GEOGRAPHICAL INFORMATION SYSTEMS / CARTOGRAPHY

EVALUATION OF TRANSITION TO UPDATED REGIONAL Q-GEOID MODEL

J. Kaminskis[1], A. Vallis[2], I. Stamure[3], M. Reiniks[4], I. Geipele[5], N. Zeltins[6]

[1, 4] Riga Technical University, Department of Geomatics
115 – 1/1 Meza Str., Riga, LV-1048, LATVIA
E-mail: janis.kaminskis@rtu.lv
[2]Ltd. Geostar,
20 Marupes street, Riga, Latvia LV-1002
[3, 5] Riga Technical University, Institute of Civil Engineering and Real Estate Economics,
6 – 210 Kalnciema Str., Riga, LV-1048, LATVIA
[6] Institute of Physical Energetics
11 Krivu Str., Riga, LV-1006, LATVIA

During the last years, the European and the Nordic quasi-geoid models and existing national q-geoid models covered the territory of Latvia. There are many ways for comparison and tests of results achieved. Scientists and professionals can compare models directly at some special geodetic co-location stations or use GNSS/ levelling sites. The results of this research can be used by scientists and specialists in the fundamental geodetic observations for independent monitoring of existing q-geoid models and evaluation of accuracy.

The research aims at evaluating the transition to the best updated regional q-geoid model. The research objectives are the following: 1) to investigate and analyse the development of q-geoid model LV14; 2) to conduct precision research; 3) to assess the challenges of the European Vertical Reference System; 4) to draw conclusions that allow for further research in this area for development and improvement.

Within the framework of the research, the authors have used a variety of research methods. Historical and logical approaches, comparative analysis and synthesis methods, as well as inductive – deductive data analysis methods have been selected for the research.

A conclusion for such kind of studies is to implement the most appropriate q-geoid solution and to develop new astrogeodetic methods for unification, monitoring and for reliability of a geodetic reference network.

Keywords: *accuracy evaluation, GNSS/levelling, q-geoid model*

1. INTRODUCTION

Now many engineering works and scientific research sectors need the accurate determination of coordinates; therefore, it is more relevant for the effective use of the Global Navigation Satellite System (GNSS) positioning technology.

All developed countries of the world have created and constantly improve land-based global and regional GNSS reference networks.

Scientific research uses the term "q-geoid", denoting the equipotential surface of the Earth's gravitational field, from which "normal height" is deducted during GNSS measurement process or some kind of innovative levelling [24].

By contrast, the term "geoid" is used, when geoid and q-geoid surface practically coincide. The Esri Support GIS Dictionary states that "geoid is a hypothetical surface representing the form the Earth's oceans would take if there were no land and the water were free to respond to the Earth's gravitational and centrifugal forces. The generated geoid is irregular, which varies from a perfect sphere by as much as 75 meters above and 100 meters below its surface" [5]. In the case of Latvia, the amplitude and precision of the output data set do not give a practical opportunity to calculate those few millimetres or centimetres that separate the geoid from q-geoid. In practice, the difference between geoid and q-geoid appears in high altitude countries, where normal height and orthometric height values by definition are distinctly different.

In 1998, a high-precision quasi-geodetic LV98 model was developed for the territory of Latvia, and its wide application in practice was started in real-time measurements and post-processing of GNSS / GPS [16]. Model LV98 is devoted to a series of research and Doctoral Theses, as well as approbated in practical geodesy. The model has been studied by specialists of different levels, who provided independently mutually consistent assessments, approving the model accuracy of 4.2 cm, 6 cm, and 8 cm. The accuracy of the model to the global models, surfaces of different height reference, local support network reference points are investigated by such scientists as W. Torge, R. Forsberg, D. Solheim, A. Kalantaite, E.K. Parseliunas, P. Petroskevicius, P. Viskontas, R. Jaeger, G. Younis, A. Ellmann, L Jivall, J. Kaminskis, I. Janpaule, J. Balodis, I. Aleksejenko, M. Kalinka, etc.[1], [2], [4], [6], [8]–[15], [17], [21], [24].

The Baltic geoid is fundamentally important for the joint interconnection of the Baltic height systems. [2], [22], but each of them requires a superior geoid model. The exact geoid model is highly topical to move closer to the European Vertical Reference System (of the EVRS) requirements and needs. In Latvia, at present, the transition from the Baltic Height System (BAS-77, Kronstadt) to the system EVRS2007 (Amsterdam pale) is approaching the final stage.

The research aims at evaluating the transition process to the best updated q-geoid model in Latvia – in the Baltic Sea region. To achieve the aim of the research, the following tasks have been set: 1) to research and analyse the development of q-geoid model LV14 in Latvia; 2) to actualize the precision research in the scientific area; 3) to assess the challenges identified by the European Vertical Reference System; 4) to draw up the main conclusions that will promote the continuation of research in this field, contributing to the development and improvement.

Within the framework of the research, the authors have used a variety of research methods. Historical and logical approaches, comparative analysis and synthesis methods, as well as inductive-deductive data analysis methods have been selected for the research.

2. DEVELOPMENT PROCESS OF Q-GEOID MODEL LV14

The main area of the research is the territory of Latvia. Latvia lies on the eastern shores of the Baltic Sea – on the north – western part of the East European platform. Figure 1 reflects the territory of Latvia with its geographical coordinates within the Nordic region.

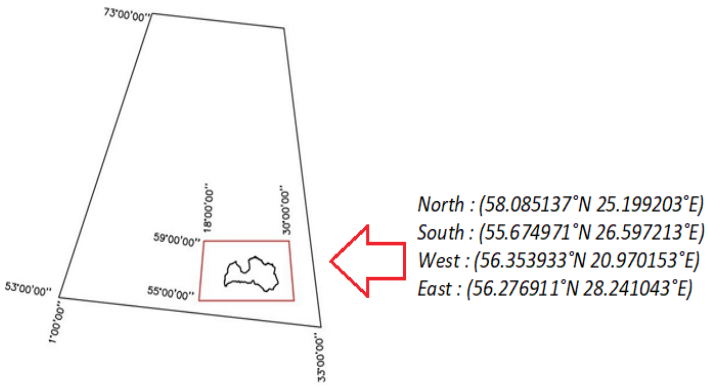

Fig. 1. Research area – the territory of Latvia in geographic coordinates [made by the authors].

Currently, the accuracy of the gravimetric geoid model LV98 in Latvia reaches 6–8 centimetres (see Fig. 2). This model is based on the use of gravimetric measurement data from the Soviet time maps and the method used in the GRAVSOFT software developed in Denmark. The developed model was a very significant achievement in the development of geodesy of Latvia, because it was the first and by 2015 the only official geoid model in Latvia.

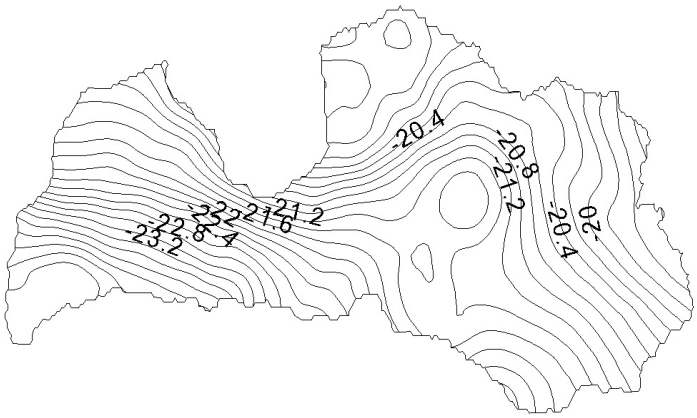

Fig. 2. Q-geoid model LV98 in Latvia. Contour interval is 0.2 m [made by the authors, visualised by the Trimble Business Center].

In the national economy of Latvia, the use of significant GNSS technological methods identifies new challenges and new precision requirements. A long period of time has passed since the establishment of LV98, and the accuracy of this geoid model is no longer in line with the precision and mass application of the GNSS measurable.

There is now a need for a more accurate geoid model operating at normal height determination, using the precision of the GNSS coordinate methods. This process demands high precision requirements of geodesy, cadastre, construction, real estate management process and other industries.

In 2012, representatives of the Geospatial Information Agency of Latvia presented the national reports providing information that to obtain a high precision levelling and GNSS measurement data Latvia would be developing a new, more accurate q-geoid model with accuracy of 1 cm [1]. Along with the development of a new and high-precision q-geoid model and despite the presence of the Baltic Sea, politicians of Latvia have taken a political decision to move to a new height system – the European Vertical Reference System.

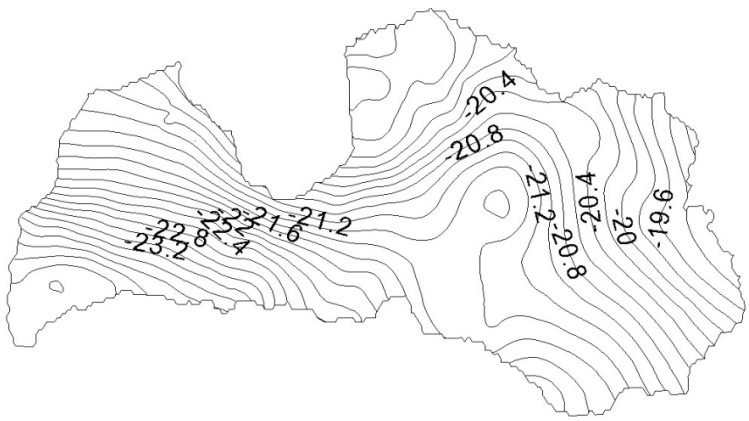

Fig. 3. Q-geoid model LV14 in Latvia. Contour interval is 0.2 m
[made by the authors, visualised by the Trimble Business Center].

The new q-geoid model LV14 (version 1) was launched in 2014 (see Fig. 3), measuring at the accuracy of 4.5 cm relative to the selected GNSS and levelling different network points. Depending on the q-geoid versions and methods of measurement accuracy, assessments occur at the accuracy of 4.3 cm, 5.3 cm and 6.6 cm. The model was designed as a checklist with irregular step length and width, close to 0.025 degrees. To develop the model, fixed points of up to 2 km behind the state border of Latvia were used.

However, after a few days the new model (version 2) was launched in the form of a regular matrix with a regular step both in length and width of 0.025 degrees. Both specified in the model LV14 versions (version 1 and version 2) cannot be used in the state sea aquarium and several places in the border area.

A short time later a rebuilt model (version 3) was launched, which covered a wider land area of Latvia (6 km beyond the border) and it was used all over the land area in Latvia.

3. Q-GEOID PATTERNS FOR ACCURACY RESEARCH

In the scientific environment, no publications have been published on the developed version of the LV14 model, there is no evidence or independently conducted tests and studies of data and methodology used for calculations. Based on the above, the authors of the research compared the different versions of the LV14 model with the previously widely used q-geoid model LV98 and the publicly available latest q-geoid models of other countries, which also include the territories of other Baltic Sea countries - Estonia, Lithuania and Sweden.

The comparison was made on the surface of the ellipsoid. Originally, it was established in point grille, which coincided with the height of the surface of a rotating ellipsoid. Trimble Business Center (version 3.40) allows its users to effectively edit, process and configure geospatial data and create accurate reports. By using different models, "normal heights" were obtained, which were further used to calculate the difference between these indicators using the spreadsheet data. The visualization of the received data was implemented with the help of Trimble Business Center.

To evaluate the accuracy of the new q-geoid model, it was compared with the model LV98, and this comparison gave a cartogram with several places in Latvia, where are observed visually a significant differences. Extremes were identified from - 2 cm in the north of Vidzeme up to + 43 cm in Kurzeme (see Fig.4).

Table 1

Differences between the Compared Models LV98 and LV14 [made by the authors]

Compared models	MEAN (m)	RMS (m)	MIN (m)	MAX (m)
LV98 and LV14 (version 3)	0.142	0.058	-0.020	0.432

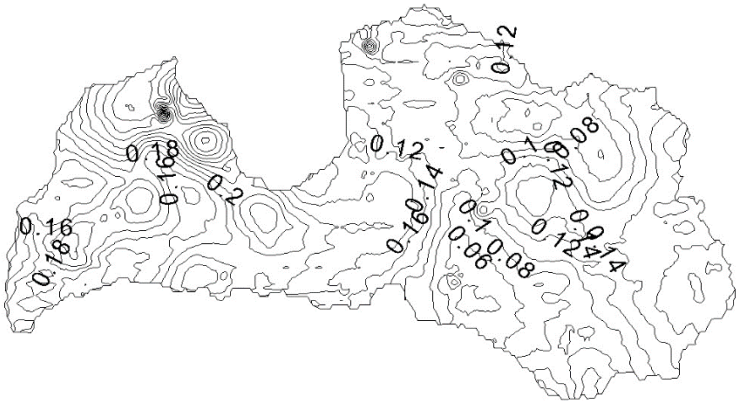

Fig. 4. Differences between q-geoid model LV98 and LV14 (version 3) in Latvia.
Contour interval is 0.2 m [made by the authors, visualised by the Trimble Business Center].

By comparing LV14 model version 3 with Sweden SWEN08_2000 q-geoid model, several significant differences can be identified (see Fig.5). Swedish high-precision q-geoid model covers the western part of the territory of Latvia and a bit of Vidzeme.

Table 2

Differences between the Compared Models SWEN08_2000 and LV14 [made by the authors]

Compared models	MEAN (m)	RMS (m)	MIN (m)	MAX (m)
SWEN08_2000 and LV14 (version 3)	-0.069	0.032	-0.176	0.090

The standard error of Swedish q-geoid SWEN08_RH2000 was estimated to be 10–15 millimetres everywhere on the Swedish mainland with exception of the small area to the north-west. The standard error is larger in the latter area and at sea, probably around 5–10 centimetres [19].

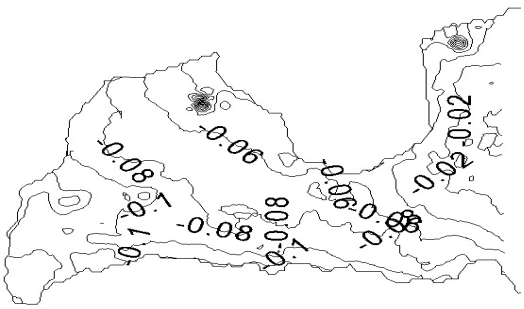

Fig. 5. Differences between q-geoid model SWEN08_2000 and LV14 (version 3) in Latvia. Contour interval is 0.2 m [made by the authors, visualised by the Trimble Business Center].

LV14 model version 3 was compared with the Estonian q-geoid model EST_GEOID2003 (see Fig. 6), which was assessed at the accuracy of 1–3 cm [20]. In addition, compared to the Swedish q-geoid model several significant differences can be identified: the Estonian precision q-geoid model covers the territory of Latvia in the northern part of Vidzeme, Latgale and a bit of Kurzeme.

Table 3

Differences between the Compared Models EST_GEOID2003 and LV14 [made by the authors]

Compared models	MEAN (m)	RMS (m)	MIN (m)	MAX (m)
EST_GEOID2003 and LV14 (version 3)	0.115	0.034	-0.009	0.276

Graphically marked problem areas were compared in Vidzeme and Kurzeme. It is important to note that the Estonian q-geoid model EST_GEOID2003 has been calculated to include the latest GNSS and levelling measurement data.

Fig. 6. Differences between q-geoid model EST_GEOID2003 and LV14 (version 3) in Latvia. Contour interval is 0.2 m [made by the authors, visualised by the Trimble Business Center].

LV14 model version 3 was compared with the Lithuanian q-geoid LITH2011 model that had been created at the same time as LV98 model and it was also assessed at the accuracy of 6–8 cm (see Fig.7).

Table 4

Differences between the Compared Models LITH2011 and LV14 [made by the authors]

Compared models	MEAN (m)	RMS (m)	MIN (m)	MAX (m)
LITH2011 and LV14 (version 3)	-0.008	0.033	-0.09	0.079

The Lithuanian q-geoid model covers the southern part of the territory of Latvia to Riga.

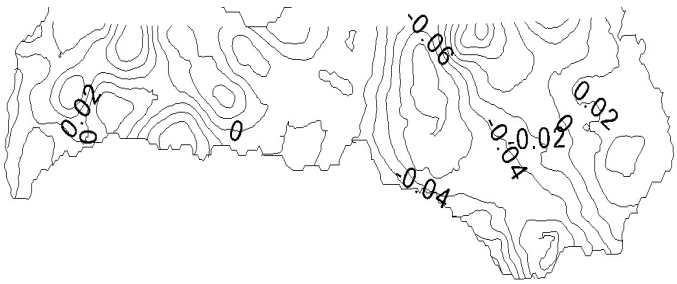

Fig. 7. Differences between q-geoid model LITH2011 and LV14 (version 3) in Latvia. Contour interval is 0.2 m [made by the authors, visualised by the Trimble Business Center].

In 2014, geodetic specialists of Estonia pointed out significant failures on the ground carried out by gravimetric measurement data within the framework of the scientific research into the development on a high surface [20]. By contrast, the only publicly available information, which gives an idea of the creation of LV14 different versions of q-geoid model and data used, is a gravimetric anomaly map of the territory of Latvia in 2014 [1]. Comparing and analysing Figs. 6 and 7, it can be concluded that according to scientists from Estonia, the new model is indicating false and incomplete data.

4. THE TRANSITION TO THE EUROPEAN VERTICAL REFERENCE SYSTEM

Due to a political decision taken to move from the BAS-77 height reference system to a height reference system of EVRS, implementation of LAS-2000.5 was carried out, which was designed for a theoretical transition algorithm [23]. A graphical representation of this algorithm is close to a linear transition from 12 cm near Daugavpils up to 17 cm near Ventspils (see Fig. 8).

Scientists have discovered that during the transition to a new height system (LAS-2000.5), the height of the highest mountain in Latvia – Gaiziņkalns – has been significantly increased during the process of data conversion. Previously, the height of Gaiziņš, according to the Baltic Height System (BAS-77), was 311.495 m, now – 311.94 m above the sea level.

Fig. 8. Data conversion algorithm from BAS-77 to LAS-2000.5 [made by the authors, visualised by the Trimble Business Center].

Highly detailed topographic information (ADTI) is mainly generated based on the heights obtained by the GNSS/GPS measurement methods using LV98 q-geoid model, while the transition algorithm does not include LV98 model. Consequently, the ADTI data introduce errors, well above the height of certainty of ADTI data. ADTI data introduce errors from -13 cm in Vidzeme to +26 cm in Kurzeme (see Fig. 9).

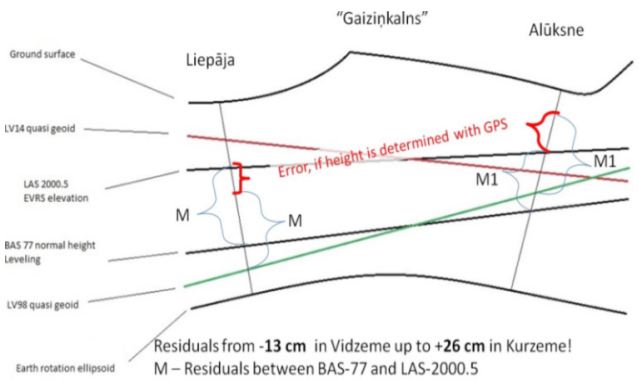

Fig. 9. Transformation algorithm errors of the highly detailed topographical data [made by the authors].

Developing ADTI data transformation algorithm, it is highly important to take into account that this type of elevation conversion does not respect the main data generation surfaces used for elevation calculations.

LV14 q-geoid model version 4 is available with the altered values and specialists' recommendations, but still there are minor bug fixes.

Table 5

Differences between the Compared Models EGM-2008 and LV14 (version 3 and version 4) [made by the authors]

Compared models	MEAN (m)	RMS (m)	MIN (m)	MAX (m)
EGM-2008 and LV14 (version 3)	-0.031	0.034	-0.214	0.094
EGM-2008 and LV14 (version 4)	-0.031	0.032	-0.124	0.050

To determine compliance with the latest European q-geoid model that is related to the height reference system of EVRS, the comparison was made with the latest and the best q-geoid model EGG 2008 (see Fig. 10).

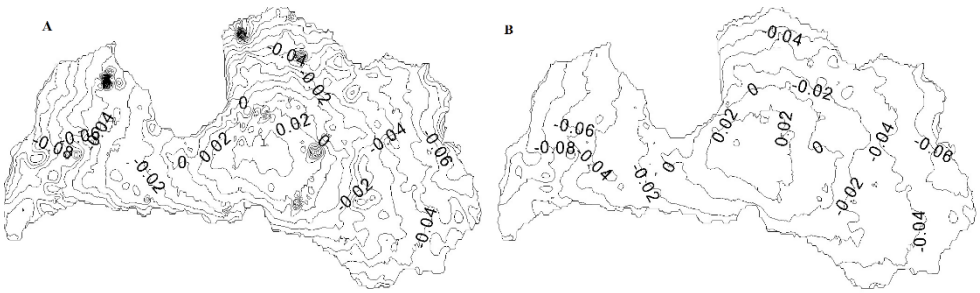

Fig. 10. Differences between q-geoid model EGM-2008 and LV14 A (version 3) and B (version 4) in Latvia. Contour interval is 0.2 m [made by the authors, visualised by the Trimble Business Center].

Analysing information in Version 3 and Version 4, it can be concluded that substantial errors are no longer visible in the model; however, there are still some problem areas, which would require more research and in-depth analysis.

5. CONCLUSIONS

Within the framework of the research, the authors have come to the following main conclusions, which will allow for further research in this area, including digital zenith camera measurements for the deflection of the vertical [17], [18]:

1. Transformation algorithm used for highly detailed topographic information or ADTI data elevation conversion does not respect the main surfaces used for elevation data generation (such as LV98).
2. Evaluating gravimetric anomalies defined in the report by the Geospatial Information Agency of Latvia on 14 November 2014 and comparing them with the Estonian report by NKG Assembly 2014 “Investigations towards the NKG2014 Geoid Model in Estonia” [20], it is clearly visible that the latest Q-geoid model LV14 contains or includes coarse gravimetric errors.
3. After transition to EVRS, in the national legislation there will still be both elevation reference surfaces – q-geoid LV98 (BAS-77/Kronstadt in the Baltic) and q-geoid LV14 (LAS2000.5/N.A.P., Amsterdam) –, and both will not have a correct transition algorithm for practitioners. The authors of the research conclude that the transition to EVRS is done in isolation from real needs and is poorly prepared.
4. Version 4 of LV14 Q-geoid model is consistent with EVRS in the range of 16 cm and it raises doubts about the effectiveness and usefulness of the elevation reference system transition.
5. Due to the implementation of a new height reference system (LAS-2000.5), the value for the highest Latvian mountain “Gaiziņkalns” also considerably grew; it was 311.495 m, now – 311.94 m above the sea level.

REFERENCES

1. Aleksejenko, I., & Kosenko K. (2012). *National Report of Latvia*. NKG Working Group on Geoid and Height System, Latvian Geospatial Information Agency. Retrieved from http://www.nkg.fi/nkg/sites/default/files/WGGHS2012_NKG_ Geoid_Heght_KKosenko.pdf.
2. Aleksejenko, I., Sakne, J., Kalinka, M., Reiniks, M., Krikstaponis, B., Parseliunas, E.K., Petroskevicius, P., & Viskontas, P. (2012). The united geodetic vertical network of Latvia and Lithuania. *Geodesy and Cartography, 38*(1), 9–19.
3. Ellmann, A. (2012). Considerations on the further improvements of regional geoid modelling over the Baltic countries. *Geodezija ir Kartografija, 36*(1), 5–15.
4. Ellmann, A. (2004). *The geoid for the Baltic countries determined by the least squares modification of Stoke's formula*. Doctoral Dissertation in Geodesy. Stocholm: Royal Institute of Technology (KTH), Department of Infrastructure.
5. Esri Support GIS Dictionary. (2017). *Definition of geoid*. Retrieved from https://support.esri.com/en/other-resources/gis-dictionary/term/geoid
6. Forsberg, R., Kaminskis, J., & Solheim, D. (1997). Geoid of the Nordic and Baltic Region from gravimetry and satellite altimetry. In J. Segawa, H. Fujimoto& S. Okubo (Eds.), *Gravity, geoid and marine geodesy*. (pp. 540–547). IAG Symp. Series, 117, Berlin: Springer.
7. International Centre for Global Earth Models. Retrieved from http://icgem.gfz-potsdam.de/ICGEM
8. Jäger, R., Kaminskis, J., Strauhmanis, J., & Younis, G. (2012). Determination of quasi-geoid as height component of the geodetic infrastructure for GNSS positioning services in the Baltic States. *Latvian Journal of Physics and Technical Sciences, 3*, 5–15.
9. Janpaule, I., Jaeger, R., Younis, G., Kaminskis, J., & Zariņš, A. (2013). DFHRS-based computation of quasi-geoid of Latvia. *Geodesy and Cartography*, *39*(1), 11–17. ISSN 2029-6991.
10. Janpaule, I. (2014). Latvijas ģeoīda modeļa precizitātes uzlabošanas iespējas. [Latvian geoid model's accuracy improvement opportunities]. In *72nd Scientific Conference of the University of Latvia, Astronomy and Geodesy Section*, 5 February 2014, Latvia.
11. Jivall, L., Kaminskis, J., & Parseliunas, E. (2008). *Improvement and extension of ETRS 89 in Latvia and Lithuania based on the NKG 2003 GPS campaign*. EUREF Publication No.16 (Band 40), (pp. 156–162), Frankfurt am Main.
12. Jürgenson, H. (2002). Estonian geoid and other reference surfaces. *Geodezija ir Kartografija, 28*(3), 108–111.
13. Jürgenson, H., Türk, K., & Randjärv, J. (2011). Determination and evaluation of the Estonian fitted geoid model EST-GEOID 2003. *Geodesy and Cartography*, *37*(1), 15–21.
14. Kaminskis, J. (2009). Apvienotais Latvijas gravimetriskais ģeoīds [Joint gravimetric geoid of Latvia]. *Geomatics*, *5*, 13–20.
15. Kaminskis, J. (2010). Geoid model for surveying in Latvia. In *International FIG Congress "Facing the Challenges – Building the Capacity"*, 10–16 April 2010 (pp. 1–7). Australia, Sidney.
16. Kaminskis, J. (2010). *Geoid model in Latvia and its development*. PhD Thesis. Riga: RTU. ISBN 978-9934-507-27-4
17. Kaminskis, J., Janpaule, I., Zarins, A., & Rothacher, M. (2016). Latvian digital zenith camera in test applications. In Proceedings of NKG 2014 General Assembly, 1–4 September 2014 (pp. 122–125). Gothenburg, Sweden, ISSN 0280-5731.
18. Kaminskis, J., Vallis, A., Geipele, I., Stamure, I., Reiniks, M., & Krutova, U. (2017). Evaluation of the updated regional transition Q-geoid model. In *EUREF Symposia 2017*, 17–19 May 2017. Wroclaw. Retrieved from http://www.euref.eu/symposia/2017Wroclaw/02-11-Kaminskis.pdf

19. Lantmäteriet, SWEN08_RH2000 & SWEN08_RH70. (2016). Retrieved from https://www.lantmateriet.se/en/Maps-and-geographic-information/GPS-and-geodetic-surveys/Geodesy/ Transformations/ Geoid-models/
20. Märdla, S. Oja, T., & Ellmann, A. (2014). *Investigations towards the NKG2014 geoid model in Estonia*. Abstract Book for the NKG General Assembly. Retrieved from https://www.lantmateriet.se/globalassets/kartor-och-geografisk-information/gps-och-matning/geodesi/rapporter_publikationer/rapporter/lantmaterirapport-2016-4-nkg-general-assembly-2014.pdf
21. Petroškevičius, P., & Paršeliūnas, E. (1995). Determination of the Lithuanian territory geoid. *Geodezija ir Kartografija*, *21*(2), 50–58.
22. Sas-Uhrynowski, A., Mroczek, S., Sas, A., Petroškevičius, P., Obuchowski, R., & Rimkus, D. (2002). Establishment of Lithuanian national gravimetric first order network. *Geodezija ir Kartografija,28*(3), 75–82.
23. Sproģis, V., & Aleksejenko, I., (2014). *Q-geoid model LV'14*. Latvian Geospatial Information Agency. Retrieved from http://www.lgia.gov.lv/~/media/LGIA/Aktual14/Kvazogeoida_modelis_LV14_ 22112014.ashx
24. Torge, W. (2001). *Geodesy* (3rd ed.). Berlin, New York: Walter de Gruyter.

KVAZIĢEOĪDA REĢIONĀLĀ MODEĻA PILNVEIDOŠANAS PROCESA NOVĒRTĒJUMS LATVIJĀ

J. Kaminskis, A. Vallis, I. Stāmure, M. Reiniks, I. Geipele, N. Zeltiņš

K o p s a v i l k u m s

Mūsdienās liela nozīme ir globālās navigācijas satelītu sistēmas pozicionēšanas tehnoloģiju racionālai un lietderīgai izmantošanai dažādās zinātnisko pētījumu un inženiertehnisko darbu jomās, kur nepieciešama precīzu pozīciju noteikšana, piemēram, nekustamā īpašuma robežu noteikšanai, kadastra datu iegūšanai, būvniecības procesu realizācijai, arī jaunu teritoriju plānojuma attīstībai, u.c. Daudzās pasaules valstīs ir izveidoti, tiek pastāvīgi uzlaboti, kā arī pilnveidoti augstas precizitātes, uz zemes bāzētie globālie un reģionālie globālās navigācijas satelītu sistēmas pastāvīgās darbības atbalsta sistēmu tīkli.

Pētījuma mērķis ir novērtēt uz uzlabotu kvaziģeoīda reģionālo modeli vērstu pārejas procesu. Pētījuma mērķa sasniegšanai nepieciešams izpētīt un analizēt kvaziģeoīda modeļa LV14 attīstību, izvērtēt esošos precizitātes pētījumus, novērtēt Eiropas vertikālās atskaites sistēmas ieviešanas problemātiku un izstrādāt galvenos secinājumus un attīstības priekšlikumus nākotnes pētījumu virzienu attīstībai un uzlabošanai kvaziģeoīda reģionālā modeļa pilnveidošanai Latvijā, t.sk. pielietojot inovatīvus astro-ģeodēziskos novērojumus.

Pētījuma izstrādes laikā ir izvēlēta vēsturiskā un loģiskā pieeja, salīdzinošā analīze un sintēzes metodes, kā arī induktīvās-deduktīvās datu analīzes metodes. Datu apstrādei un informācijas vizualizācijai izmantota Trimble Business Center programmatūra.

16.03.2018.